

## Intercomparison of cloud condensation nuclei and hygroscopic fraction measurements: Coated soot particles investigated during the LACIS Experiment in November (LExNo)

J. R. Snider,<sup>1</sup> H. Wex,<sup>2</sup> D. Rose,<sup>3</sup> A. Kristensson,<sup>4,5</sup> F. Stratmann,<sup>2</sup> T. Hennig,<sup>2,6</sup> S. Henning,<sup>2</sup> A. Kiselev,<sup>2</sup> M. Bilde,<sup>4</sup> M. Burkhardt,<sup>1</sup> U. Dusek,<sup>3,7</sup> G. P. Frank,<sup>3,5</sup> A. Kiendler-Scharr,<sup>8</sup> T. F. Mentel,<sup>8</sup> M. D. Petters,<sup>9,10</sup> and U. Pöschl<sup>3</sup>

Received 6 September 2009; revised 5 February 2009; accepted 1 March 2010; published 4 June 2010.

[1] Four cloud condensation nuclei (CCN) instruments were used to sample size-selected particles prepared at the Leipzig Aerosol Cloud Interaction Simulator facility. Included were two Wyoming static diffusion CCN instruments, the continuous flow instrument built by Droplet Measurement Technologies, and the continuous flow Leipzig instrument. The aerosols were composed of ammonium sulfate, levoglucosan, levoglucosan and soot, and ammonium hydrogen sulfate and soot. Comparisons are made among critical supersaturation values from the CCN instruments and derived from measurements made with a humidified tandem differential mobility system. The comparison is quite encouraging: with few exceptions the reported critical supersaturations agree within known experimental uncertainty limits. Also reported are CCN- and hygroscopicity-based estimates of the soot particles' solute fraction. Relative differences between these are as large as 40%, but an error analysis demonstrates that agreement within experimental uncertainty is achieved. We also analyze data from the Droplet Measurement Technologies and the two Wyoming static diffusion instruments for evidence of size distribution broadening and investigate levoglucosan particle growth kinetics in the Wyoming CCN instrument.

**Citation:** Snider, J. R., et al. (2010), Intercomparison of cloud condensation nuclei and hygroscopic fraction measurements: Coated soot particles investigated during the LACIS Experiment in November (LExNo), *J. Geophys. Res.*, 115, D11205, doi:10.1029/2009JD012618.

### 1. Introduction

[2] Aerosols emitted into the atmosphere from combustion, and their effect on cloud properties and precipitation, have been the subject of research for several decades. A seminal publication is the observation of clouds contami-

nated by aerosol emissions from sugar cane fires [Warner and Twomey, 1967]. That study established the hypothesis that an increased abundance of aerosol particles may inhibit the development of precipitation. Particle abundance is also known to mediate cloud reflection of solar radiation (cloud albedo [Twomey, 1974]) and both processes are being scrutinized as drivers of climate change [Levin and Cotton, 2009; Stevens and Feingold, 2009]. Investigations of aerosol source processes demonstrate that biomass and fossil fuel combustion are dominant sources of the submicrometric particles likely to influence both precipitation and cloud albedo (for a review, see Wallace and Hobbs [2006]). That dominance is evident in the consideration given to aerosol generated by combustion in global models [Textor et al., 2006].

[3] As is the case for all aerosol types, connecting the size and concentration of combustion particles to their effect on cloud albedo and precipitation requires additional information. A useful ingredient is the fraction of the dry particulate volume occupied by hygroscopic substances; material which promotes water uptake at relative humidities below saturation. In addition to being a determinant of the concentration of droplets formed in a cloud updraft [Fitzgerald, 1974], hygroscopic materials also impact visibility [Fitzgerald et al., 1982; McMurry and Stolzenburg, 1989] and direct

<sup>1</sup>Department of Atmospheric Science, University of Wyoming, Laramie, Wyoming, USA.

<sup>2</sup>Institute for Tropospheric Research, Department of Physics, Leipzig, Germany.

<sup>3</sup>Biogeochemistry Department, Max Planck Institute for Chemistry, Mainz, Germany.

<sup>4</sup>Department of Chemistry, University of Copenhagen, Copenhagen, Denmark.

<sup>5</sup>Now at Department of Physics, Lund University, Lund, Sweden.

<sup>6</sup>Now at Institute for Applied Environmental Science, Stockholm University, Stockholm, Sweden.

<sup>7</sup>Now at Institute for Marine and Atmospheric Research, Utrecht University, Utrecht, Netherlands.

<sup>8</sup>ICG-II: Troposphere, Juelich Research Centre, Juelich, Germany.

<sup>9</sup>Department of Atmospheric Science, Colorado State University, Fort Collins, Colorado, USA.

<sup>10</sup>Now at Department of Marine, Earth and Atmospheric Science, North Carolina State University, Raleigh, North Carolina, USA.

aerosol forcing of climate [Boucher and Anderson, 1995]. Both hygroscopic and nonhygroscopic materials are recognized as significant components of particulate emitted from combustion sources [Andreae et al., 1988; Lightly et al., 2000].

[4] Here we report on laboratory studies which used four cloud condensation nuclei (CCN) measurement systems, and an aerosol hygroscopicity measurement system, to characterize aerosols synthesized to mimic the condensed products of combustion. These studies, hereafter referred to as the LACIS Experiment in November (LExNo), employed an apparatus which thermally condensed either ammonium sulfate or levoglucosan onto particles composed of soot. We report on measurements of the coated soot particles' CCN activity and their solute fraction. The synthesized particles are thought to approximate particles emitted directly into the atmosphere from biomass burning (soot-levoglucosan particles) or that result from atmospheric processing of particulate derived from fossil fuel combustion (soot-ammonium sulfate particles) [Stratmann et al., 2010]. Also investigated were particles composed solely of either ammonium sulfate or levoglucosan; analysis of these experiments allowed us to quantify CCN measurement errors. Our analysis of the LExNo data set is underlain by a Köhler model used to calibrate supersaturation in the CCN chambers and to facilitate comparison of the hygroscopicity and CCN data sets.

[5] Other papers reporting on the LExNo include a description of the aerosol generation apparatus [Stratmann et al., 2010], an analysis of particle chemical composition and its comparison via Köhler theory to hygroscopicity and CCN properties [Henning et al., 2010], and an analysis of particle density and morphology [Kiselev et al., 2010]. All of these companion studies report that the chemical composition of the soot-ammonium sulfate particles was actually soot internally mixed with ammonium hydrogen sulfate, plus an organic material which was tentatively identified as 2-propanol. The vapor phase of the latter substance was adsorbed onto soot particles produced during some experiments, causing them to be more compact [Kütz and Schmidt-Ott, 1992; Kiselev et al., 2010]. The transformation of ammonium sulfate to ammonium hydrogen sulfate is thought to have occurred during the thermal condensation of ammonium sulfate onto the soot. In spite of the divergence between the chemical identity of the sulfate-containing material used in the particle synthesis system, and that derived by mass spectrometry [Stratmann et al., 2010], we refer to the resulting particles as being soot coated with ammonium sulfate (soot-ammonium sulfate particles).

[6] In addition to providing results commensurate with broader LExNo goals, for example our investigations of the solute fraction carried by coated soot particles (section 6.6), we compare measurements reported by four CCN instruments. The basis for the CCN comparisons is the particles' critical supersaturation (sections 6.2 and 6.6) and the width of their distribution function (section 6.3). The comparison required calibration of the supersaturation established within the CCN chambers (section 3.2) and measurement of the supersaturation-dependent CCN activity (section 5.2). Prior laboratory CCN comparison studies are reported by Jiusto et al. [1981] and Hudson and Alofs [1981]; relative to that

work we document significant improvement in the determination of the critical supersaturation (section 8).

## 2. CCN Instruments

[7] Descriptions of the CCN instruments used during LExNo are published and will not be repeated here [Stratmann et al., 2004; Roberts and Nenes, 2005; Snider et al., 2006]. However, we will discuss, and contrast, the physics underlying the production of supersaturated conditions, the duration of time that aerosol is exposed to supersaturated conditions and the methodology used to relate the operational state of a CCN chamber to the occurrence of heterogeneous cloud droplet nucleation. Throughout this paper we refer to this particular nucleation process as "activation." Figure 1 shows vertical cross sections of the three CCN devices. The Laramie and Copenhagen groups both operated a Wyoming static diffusion instrument, the Leipzig group used their continuous flow instrument, and the Mainz group used the Droplet Measurement Technologies continuous flow instrument (DMT-CCNC). We refer to these as the "Wyoming," "Leipzig" and "Mainz" CCN instruments.

[8] In Figure 1 the vectors indicate the direction and magnitudes of the sensible and latent heat fluxes. For the Wyoming static diffusion instrument, it is assumed that the fluxes are uniform in space (nondivergent) and that lateral wall effects are negligible. It is also assumed that fluxes do not vary with time (steady state assumption [see Katz and Mirabel, 1975]). The uniform and steady flux assumptions lead to solutions of the one-dimensional heat and vapor mass diffusion equations. There are three important characteristics of these: (1) the temperature profile (in the vertical dimension) is approximately linear, (2) the vapor partial pressure profile is approximately linear [Katz and Mirabel, 1975], and (3) the saturation vapor pressure profile is nonlinear. These characteristics lead to the parabolic steady state supersaturation profile illustrated in Figure 1. The center of the chamber is illuminated with a laser and scattering produced by the activating particles is detected and related to CCN concentration via a calibration [Gras, 1995; Delene and Deshler, 2000; Snider et al., 2006].

[9] Within the cylindrical Leipzig and Mainz flow tubes the aerosol stream is confined, by sheath airflow, to the tube centerline. Focusing on energy transport occurring perpendicular to the centerline of the Leipzig tube (Figure 1), the modeling study of Stratmann et al. [2004] demonstrates that the Leipzig instrument produces divergent fields of sensible and latent heat flux. In response to the sensible heat flux divergence the aerosol stream experiences decreasing temperature, particularly in the upper 20% of the flow tube. Cooling drives an increase in relative humidity and this increase occurs in spite of the divergent latent heat flux. The latent and sensible heat flux divergences do diminish with downstream distance as the flow properties relax to the uniform boundary condition imposed by the tube wall. The model of Stratmann et al. also shows that the maximum chamber supersaturation is produced approximately halfway down from the top of the tube. This maximum increases with increasing humidity of the aerosol and sheath streams, and with decreasing wall temperature. The flow stream humidities are established in humidifiers operated upstream

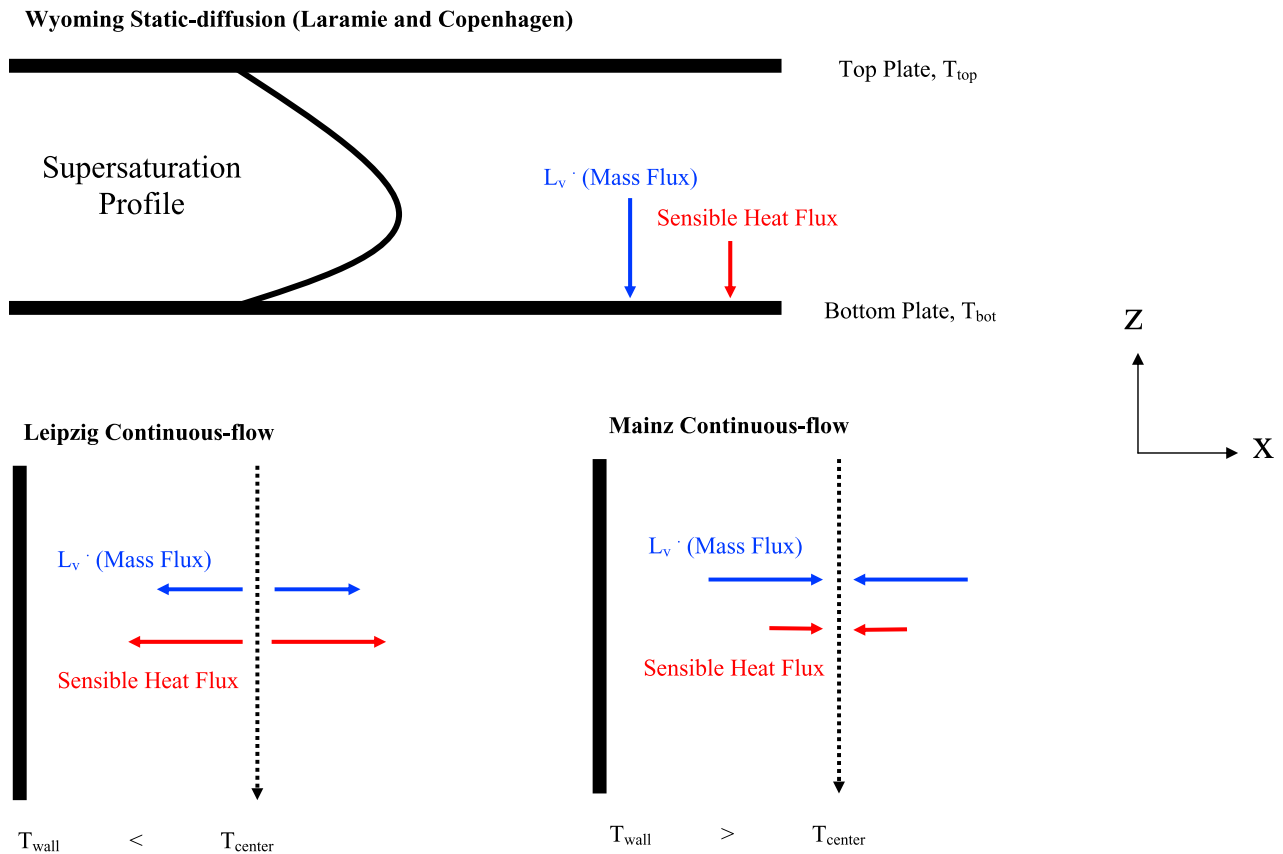


**Figure 1.** Vertical cross sections of the Wyoming static diffusion chamber, the Leipzig continuous flow chamber, and the Mainz continuous flow chamber.

of the Leipzig flow tube. During LExNo the particle residence time in the aerosol humidifier, which saturates that flow stream at 19°C, and in tubing which transports the humidified aerosol flow stream to the top of the flow tube were 2.0 and 1.5 s, respectively.

[10] Focusing now on the schematic of the Mainz instrument, we note that the latent and sensible heat fluxes are convergent along the tube centerline. This means that

the aerosol flow stream is both heated, and humidified, as it moves down the tube. Three other aspects of the Mainz instrument differ from the Leipzig. First, there are three tube heaters positioned at the top (heater 1), the waist (heater 2) and bottom (heater 3) of the Mainz flow tube. These heaters, and the heater control system, produce the condition  $T_1 < T_2 < T_3$  with the topmost streamwise temperature gradient, between heaters 1 and 2, slightly larger

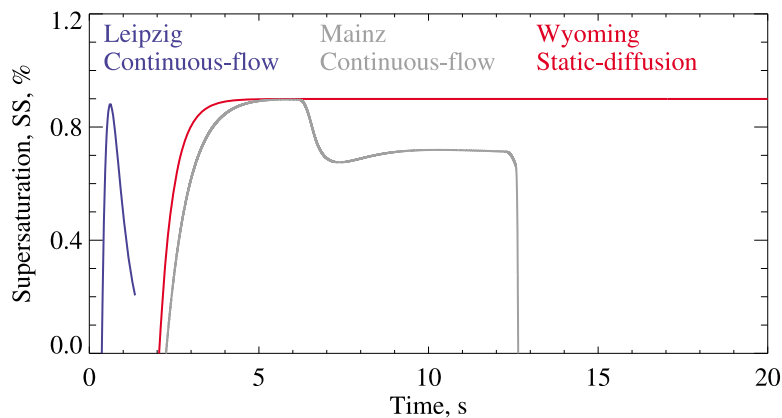


**Figure 2.** Time-dependent supersaturations based on models of the Leipzig continuous flow, Mainz continuous flow, and the Wyoming static diffusion CCN chambers. In the case of the Leipzig and Mainz instruments the supersaturation along the tube centerline is reported, starting at the tube entrance and ending at the tube exit. In the case of the Wyoming chamber the supersaturation halfway between the top and bottom plates is reported, starting at the beginning of the 20 s detection interval.

**Table 1.** Conditions for Modeling the Time-Dependent Chamber Supersaturation Profiles in Figure 2

Instrument	Temperature, <sup>a</sup> °C	Pressure, hPa	Gas Flow Rates, <sup>b</sup> alpm	Fractional Relative Humidities at Inlet
Leipzig continuous flow	19.60, 12.35 <sup>c</sup>	1000	Sheath: 4.00 Aerosol: 0.08	Sheath: 0.96 <sup>d</sup> Aerosol: 0.96 <sup>d</sup>
Mainz continuous flow	22.60, 28.53, 33.50 <sup>e</sup>	1000	Sheath: 0.45 Aerosol: 0.05	Sheath: 0.94 Aerosol: 0.10
Wyoming static diffusion	19.60, 15.06 <sup>f</sup>	1000	Not applicable	0.10

<sup>a</sup>Temperature is reported with 0.01°C precision because of model sensitivity to the temperature boundary conditions. In practice, temperature is not measured with 0.01°C precision.

<sup>b</sup>Unit alpm is actual liters per minute.

<sup>c</sup>Gas temperatures at tube entrance and at wall.

<sup>d</sup>Humidified mixture of 0.98 mole fraction dry air and 0.02 mole fraction helium.

<sup>e</sup>Temperatures of top, waist, and bottom zones. Air entering the top of the flow tube (aerosol and sheath flows) is at 22.60°C.

<sup>f</sup>Temperatures of the top and bottom plate.

than the gradient between heaters 2 and 3. Second, the tube wall is wetted with a water handling system, which differs from the situation inside the Leipzig instrument, where the tube wall is wetted by condensation. Third, there is no pre-humidification of the aerosol flow stream; this flow entered the top of the Mainz tube with the fractional relative humidity of the LExNo aerosol (section 3.1). A similarity for the Mainz and Leipzig instruments is the prehumidification of the sheath flow streams that occurs upstream of the flow tube.

[11] Time-dependent predictions of the chamber supersaturation, along the tube centerline (Mainz and Leipzig instruments) and halfway between the parallel plates of the Wyoming chamber, are presented in Figure 2. The computational methods used to generate these profiles are described by *Stratmann et al.* [2004] (Leipzig instrument), by *Saxena et al.* [1970] (Wyoming instrument) and by *Press et al.* [1992] (Mainz instrument). Model boundary conditions are provided in Table 1. Figure 2 shows that the interval of particle exposure to the maximum chamber supersaturation differs among instruments with the smallest value in the Leipzig instrument and the largest in the Wyoming. Since this time interval has been proposed as a factor influencing what a CCN instrument reports, particularly for an aerosol containing an organic component [*de Oliveira and Vali*, 1995; *Chuang et al.*, 1997; *Shantz et al.*, 2003; *Stroud et al.*, 2007; *Asa-Awuku et al.*, 2009], this issue is examined in greater detail in section 7 and in the auxiliary material.<sup>1</sup> There we examine the conjecture that a short interval of exposure to the maximum chamber supersaturation leads to an overestimation of the supersaturation corresponding to particle activation.

[12] In addition to the consideration of the time dependence of the supersaturation given in the previous paragraph, it should be recognized that activated particles (droplets) sediment a distance comparable to the height of the illuminating laser beam in the Wyoming CCN instrument (0.002 m [*Snider et al.*, 2006]). During the 20 s detection interval in the Wyoming instrument, light scattering increases due to droplet growth by condensation, reaches a maximum, and then decreases as the droplet concentration is decreased by sedimentation [*de Oliveira and Vali*, 1995]. For a maximum chamber supersaturation of 0.9%, *Delene and Deshler* [2000] show that activated droplets are resident in the laser beam for ~9 s. Referring back to Figure 2, and accounting for the supersaturation transient in the

Wyoming instrument (i.e.,  $t < 3$  s), it is concluded that the duration of particle exposure to the maximum supersaturation is larger in the Wyoming instrument (~6 s) in comparison with the Mainz (~2 s) and Leipzig instruments (~0.2 s). The first of these values increases to ~8 s when the Wyoming instrument is operated with a maximum chamber supersaturation representative of the LExNo experiments (0.5%).

### 3. Experimental Methods

[13] The purpose of this section is to describe those aspects of the LExNo experimentation germane to this study, including the preparation of the aerosols, the calibration of the maximum chamber supersaturation, the measurement of the particles' hygroscopicity, and the supersaturation scanning strategy employed by investigators from Laramie, Copenhagen and Mainz. A broader description of LExNo is provided by *Stratmann et al.* [2010].

#### 3.1. Particle Synthesis

[14] Aerosols were synthesized by two techniques during LExNo (Table 2). In the first, the particles were produced by spray atomization of solute/water solutions; the resulting polydisperse aerosols were dried, charge neutralized, size selected and diluted. Size selection was achieved within a Vienna-type electrostatic classifier [*Winklmayr et al.*, 1991] operated with aerosol and sheath flows of 1 and 10 actual liters per minute (alpm). The mobility-equivalent dry diameter of the size-selected particles was varied between 35 and 95 nm. In some of these experiments the test particle concentration was measured with a Model 3010 and a Model 3025 condensation particle counter (CPC; TSI, Inc) and in some experiments only a Model 3010 CPC was employed. Hereafter, we will refer to the CPC concentration measurement as "CN." The second particle synthesis technique involved the thermal condensation of solute onto soot particles. Between the spark discharge used to produce the soot particles, and one of two thermal condensation ovens, the option of compacting the soot particles by exposing them to 2-propanol vapor was exercised in some experiments [*Stratmann et al.*, 2010]. Both the uncompacted, and the propanol-compacted particles, were size-selected 2 times: (1) within an electrostatic classifier that was operated subsequent to the propanol compaction step (propanol-compacted particles), or subsequent to a bypass around the propanol compaction step (uncompacted particles), and (2) within an electrostatic classifier operated downstream of the thermal condensation oven. The particles extracted from the second electrostatic classifier (Vienna-type electrostatic

<sup>1</sup>Auxiliary materials are available in the HTML. doi:10.1029/2009JD012618.

**Table 2.** LExNo Experiments

Particle Synthesis Technique	Particle Type	Experiment Number	$D_g$ , nm	HHTDMA Available at RH = 0.98	Participating CCN Instruments <sup>a</sup>	Intraexperiment $SS_c$ Dispersions <sup>b</sup>
Spray atomization	ammonium sulfate	42	50	No	LAR, MAI, LEI	0.01
		43	75	No	LAR, MAI, LEI	0.02
		44	95	No	LAR, COP, MAI, LEI	0.04
		45	75	No	LAR, COP, LEI	0.01
		46	50	No	LAR, COP	NA
Spray atomization	levoglucosan	54	50	Yes	LAR, COP, MAI, LEI	0.06
		55	75	Yes	LAR, COP, MAI, LEI	0.10
		57	95	Yes	LAR, COP, MAI, LEI	0.14
Thermal condensation onto spark-generated soot	soot-uncompacted-levoglucosan	48	84	No	LAR, COP, MAI, LEI	0.05
		49	84	No	LAR, COP, MAI, LEI	0.10
		50	84	Yes	LAR, COP, MAI, LEI	0.06
		51	84	Yes	LAR, COP, MAI, LEI	0.03
		52	84	Yes	LAR, COP, MAI	0.02
		60	84	Yes	LAR, COP, MAI, LEI	0.08
Thermal condensation onto spark-generated soot	soot-uncompacted-ammonium sulfate	62	95	Yes	LAR, COP, MAI, LEI	0.10
		63	84	Yes	LAR, COP, MAI, LEI	0.08
		64	84	Yes	LAR, COP, MAI, LEI	0.10
		73	84	Yes	COP, MAI	NA
		81	84	Yes	COP, MAI, LEI	0.04
		82	84	Yes	COP, MAI	NA
Thermal condensation onto spark-generated soot	soot-compacted-ammonium sulfate	74	84	Yes	COP, MAI	NA
		75	84	Yes	COP, MAI	NA
		78	84	Yes	COP	NA
		80	84	Yes	COP, MAI	NA
		82	84	Yes	COP, MAI, LEI	0.03
Thermal condensation onto spark-generated soot	soot-compacted-levoglucosan	84	84	Yes	COP, MAI, LEI	0.03
		85	84	Yes	COP, MAI, LEI	0.06
		86	84	Yes	COP, MAI, LEI	0.10

<sup>a</sup>LAR, Laramie static diffusion; COP, Copenhagen static diffusion; MAI, Mainz continuous flow; LEI, Leipzig continuous flow.

<sup>b</sup>Derived as  $\sigma/(\overline{SS_c})$ , where  $\langle \overline{SS_c} \rangle = \frac{1}{N} \sum SS_{c,i}$ ,  $\sigma = \sqrt{\frac{1}{N-1} \sum ((SS_c)_i - \overline{SS_c})^2}$  and  $N$  is the number of CCN instruments that reported a value of  $SS_c$ . Only experiments with more than two participating instruments were used to evaluate the intraexperiment dispersion. NA denotes not available.

classifier, 1-to-10 aerosol to sheath flow ratio), at a mobility-equivalent diameter equal to 84 nm, were diluted prior to continuous monitoring by a Model 3010 CPC, a Model 3025 CPC, the CCN instruments and a high-humidity tandem differential mobility analyzer (HHTDMA).

[15] Both the soot particles treated via the propanol compaction step, and those bypassed around it, were passed through a propanol vapor remover prior to entry into the first electrostatic classifier. The vapor remover brought the particles within  $\sim 1$  mm of activated charcoal and decreased the propanol partial pressure to a value substantially less than that produced during the propanol compaction step ( $\sim 50$  hPa).

[16] Aerosol entering the Laramie, Copenhagen and Mainz CCN instruments had a humidity which depended on the synthesis technique. When expressed as a fractional relative humidity this value was approximately  $RH = 0.1$  and  $RH = 0.01$  for the pure solute and coated soot aerosols, respectively. Both aerosol types (pure solute and coated soot) entered the Leipzig flow tube preconditioned at  $RH = 0.96$  (Table 1).

### 3.2. Calibration of the Maximum Chamber Saturation

[17] Accurate determination of the maximum supersaturation achieved in the CCN chambers is an important objective of this work. This is challenging because thermal gradients are known to exist between the location where temperature is measured, within the wall of a CCN chamber, and the interior of the chamber [Snider et al., 2006; Lance et al., 2006]. Furthermore, even if the air temperature and the  $H_2O$  vapor density could be measured at the location within

the chamber where the supersaturation maximizes, measurement error can propagate into an unacceptable error in the derived supersaturation [Chylek and Wong, 1998; Snider et al., 2006]. We overcome these impediments by calibrating the chambers using size-selected test particles of ammonium sulfate. We define the “nominal” supersaturation as the maximum supersaturation calculated from the static chambers’ wall temperature [Katz and Mirabel, 1975; Snider et al., 2006], Leipzig’s wall temperature [Stratmann et al., 2004; Wex et al., 2006] and Mainz’s streamwise wall temperature difference ( $\Delta T = T_3 - T_1$  [Roberts and Nenes, 2005; Lance et al., 2006; Rose et al., 2008]). Throughout this work the critical supersaturation of a particle is symbolized as  $SS_c$  and expressed in percent units, i.e.,  $SS_c = 100 \times (RH_c - 1)$  where  $RH_c$  is the critical fractional relative humidity derived by application of a Köhler theory model (section 4). To calibrate a chamber, the nominal supersaturation that produces activation of a test particle is plotted versus the critical supersaturation ( $SS_c$ ) derived from the Köhler model and we refer to the fit of nominal supersaturation versus  $SS_c$  data as the “chamber supersaturation calibration.” Table 3 presents the outcome of those calibrations and sections 5 and 6 discuss application of the calibrations to the LExNo data set.

### 3.3. Hygroscopicity Measurements

[18] Data from the high-humidity tandem differential mobility analyzer (HHTDMA) described by Hennig et al. [2005] was also analyzed. With one exception, discussed in section 6.4, the HHTDMA measurements were acquired simultaneous with the LExNo CCN measurements. The

**Table 3.** CCN Instruments, Chamber Supersaturation Calibration, and Supersaturation Error

Type	Operating Institution	Supersaturation Calibration, %	Supersaturation Error, %
Wyoming static diffusion (SN: CCNC-100A-104) <sup>a</sup>	Department of Atmospheric Science University of Wyoming, Laramie, USA	SS = 0.62 · SS <sub>nom</sub> <sup>b</sup>	δ <sub>SS</sub> = 0.05 · SS
Wyoming static diffusion (SN: CCNC 100A-107) <sup>a</sup>	Department of Chemistry University of Copenhagen, Denmark	SS = 0.70 · SS <sub>nom</sub> <sup>b</sup>	δ <sub>SS</sub> = 0.18 · SS
Mainz continuous flow <sup>c</sup> (DMT-CCNC, SN: 02/05/0011) <sup>a</sup>	Max Planck Institute for Chemistry Mainz, Germany	SS = 0.075 · ΔT – 0.050 <sup>d</sup>	δ <sub>SS</sub> = 0.03 · SS
Leipzig continuous flow <sup>e</sup> (SN: not applicable) <sup>a</sup>	Leibniz Institute for Tropospheric Research Leipzig, Germany	SS = 38.5 – 5.83 · T <sub>w</sub> + 0.221 · T <sub>w</sub> <sup>2</sup> <sup>f</sup>	δ <sub>SS</sub> = 0.05 · √SS

<sup>a</sup>SN is the serial number of the instrument. Since the Leipzig instrument is unique, this is not relevant for the Leipzig instrument.

<sup>b</sup>SS<sub>nom</sub> is the “nominal” supersaturation computed from measurements of the difference between the bottom and top plate temperatures according to the model of *Katz and Mirabel* [1975]. The aerosol entering the Laramie and Copenhagen chambers was at the fractional relative humidity of the LExNo aerosol (0.01 ≤ RH ≤ 0.1, section 3.1).

<sup>c</sup>The Mainz instrument was operated with 0.45 and 0.05 alpm sheath and aerosol flow rates, respectively. The temperature of the sheath and aerosol streams, at the column entrance, was 22.6°C. The sheath flow stream had a fractional RH = 0.94 and the aerosol flow stream had the fractional relative humidity of the LExNo aerosol (0.01 ≤ RH ≤ 0.1, section 3.1).

<sup>d</sup>ΔT = T<sub>3</sub> – T<sub>1</sub> is the difference between temperatures maintained at the inlet and exit of the Mainz flow tube.

<sup>e</sup>The aerosol and sheath flow rates were 4.0 and 0.1 alpm, respectively. The temperature and dew point temperature of the aerosol and sheath flows were 19.6° and 19.0°C, respectively. Both flows were a humidified mixture of 0.98 mole fraction dry air and 0.02 mole fraction helium.

<sup>f</sup>T<sub>w</sub> is the Leipzig instrument wall temperature.

fractional relative humidity of the measurements was typically 0.98 but varied from experiment to experiment by as much as 0.002 fractional RH units. For the error in the nominal fractional RH we use the limits reported by *Hennig et al.* [2005]; i.e., RH – 0.012 to RH + 0.012.

### 3.4. Supersaturation Scanning Strategies

[19] Each LExNo experiment lasted approximately 1 h and during that time interval the HHTDMA and the four CCN instruments sampled the test aerosol. Different supersaturation scanning strategies were employed with the supersaturation increment equal to approximately 0.01% for the Copenhagen, no smaller than 0.01% for the Mainz, and no smaller than 0.02% for the Laramie instrument.

## 4. Köhler Model, Inputs, and Derived Quantities

[20] Here we describe the development of a Köhler model capable of reproducing the prediction of an exact model, but also sufficiently flexible for our analysis of the LExNo data set. Theoretical rigor is necessary since we use the model in analyses of equilibrium water uptake and of activation. These objectives necessitate an accounting of the non-ideality of water solute solutions at RH = 0.98 and also at the Köhler curve critical point where, in spite of the larger degree of solute dilution, the behavior of water solute systems can depart substantially from ideality. Our other requirement is that the model can be initialized with a set of measured properties and yield the dependent property without recourse to a lookup table or to curve fitting. We will also demonstrate that the requirement of flexibility leads to approximation, yet we evaluate the extent of this limitation and show how it compares to measurement error.

### 4.1. Exact and Working Köhler Models

[21] Recognizing the demands of the chamber supersaturation calibration, and our analysis of the LExNo data set, we developed a Köhler model via the following path. We start with an exact formulation of the Köhler curve and use it to calculate relationships among RH, wet particle diameter ( $D_w$ ) and dry particle diameter ( $D_d$ ) for RH = 0.98 and at the Köhler curve critical point. Once established, the exact

model is used to tune a parameter in the “working Köhler model.” It is the working Köhler model that we exercise in the chamber supersaturation calibration and in our analysis of the CCN and HHTDMA measurements.

[22] In the exact Köhler formulation we employ the expression developed by *Mita* [1979]. This relates the fractional relative humidity over a solution droplet (RH) to three composition-dependent solution properties: water activity ( $a(\text{wf})$ ), partial specific volume of water in solution ( $v(\text{wf})$ ) and the air/solution surface tension ( $\sigma(\text{wf})$ ).

$$\text{RH} = a(\text{wf}) \cdot \exp\left(\frac{4M_w}{RT} \cdot v(\text{wf}) \cdot \frac{\sigma(\text{wf})}{D_w(\text{wf}, D_d)}\right). \quad (1a)$$

Here “wf” is the weight fraction of solute in solution,  $M_w$  the molecular mass of water,  $R$  the universal gas constant,  $T$  the absolute temperature and  $D_w$  is the wet particle diameter. The equation describing the dependence of  $D_w$  on solute weight fraction and dry particle diameter, seen explicitly in equation (1a), is easily derived if it is assumed that the dry particle is a compact sphere, if all solute is dissolved and if the solution density is parameterized as a function of solute weight fraction ( $\rho(\text{wf})$ ).

[23] Since we employ data which expresses solution composition in terms of weight fraction, and also in terms of solute mole count per kilogram of water (molality), a second equation is needed to complete the exact Köhler formalism. Equation (1b) describes the relationship among weight fraction, molecular mass of the solute ( $M_s$ ) and solution molality ( $m$ ),

$$m = \frac{\text{wf}}{M_s \cdot (1 - \text{wf})}. \quad (1b)$$

[24] The exact model relies on the following sets of tabulated and parameterized property data for ammonium sulfate:  $a(m)$  [*Young and Warren*, 1992; *Low*, 1969];  $\sigma(m)$  [*Seinfeld and Pandis*, 1998]; and  $\rho(\text{wf})$  [*Tang and Munkelwitz*, 1994]. The water activity data for levoglucosan [*Svenningsson et al.*, 2006] was derived from humidified tandem differential mobility measurements and is therefore

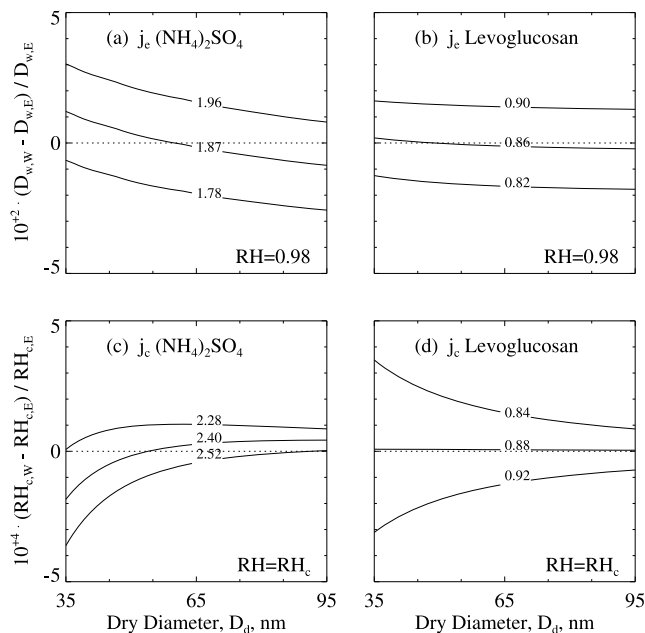


**Figure 3.** Relative departures between the working and exact Köhler models. The tuning parameter used for our analysis is shown labeling the middle line in each plot. Results obtained using a  $j_e$  or  $j_c$  value 5% larger or 5% smaller are also illustrated.

subject to larger uncertainty when compared with the tabulated, or parameterized, bulk water ammonium sulfate activity data sets. We also employ the  $\sigma(m)$  parameterization of *Svenningsson et al.* [2006] for levoglucosan. For ammonium sulfate the partial specific volume of water was derived from the  $\rho(\text{wf})$  parameterization; however, for levoglucosan volume additivity was assumed. With that assumption the partial specific volume of water is equal to the specific volume of pure water [*Brechtel and Kreidenweis*, 2000]. Equations (1a) and (1b), what we refer to as the “exact Köhler model,” were used to evaluate the  $D_w$  corresponding to a  $D_d$  ( $\text{RH} = 0.98$ ) or the critical point relative humidity ( $\text{RH}_c$ ) corresponding to a  $D_d$ .

[25] Our analysis uses a simplified Köhler model, the “working Köhler model,” which we tuned to the exact model. For the tuning parameter we use a quantity akin to the Van’t Hoff factor ( $i$ ), familiar to many in the aerosol and cloud physics communities [see, e.g., *McDonald*, 1953]. For an infinitely dilute solution, the “ideal” limit,  $i$  represents the mole count of solute entities originating from one mole of dissolved solute. We demonstrate in the Appendix that for situations with fractional relative humidity equal to or larger than  $\text{RH} = 0.98$ , the tuning parameter, symbolized by “ $j$ ,” approximates the Van’t Hoff factor.

[26] The working Köhler model we apply in our analysis of pure solute aerosols is a set of three equations. The first (equation (2a)) describes an equilibrium at  $\text{RH} = 0.98$  and contains the parameter  $j_e$  which we adjusted to force the best possible agreement with the exact model. The second formulation is for the situation at the critical point (equations (2b) and (2c)) and contains  $j_c$  which we also adjusted to force the best possible agreement with the exact model. Note that the critical point of the Köhler curve is specified by the set of

equations (2b) and (2c); that is, the latter is the derivative of the former, set to zero.

$$\text{RH} = \exp\left(\frac{4M_w\sigma_w}{RT\rho_w} \cdot \frac{1}{D_w} - j_e \cdot \frac{\rho_s M_w}{\rho_w M_s} \cdot \frac{D_d^3}{(D_w^3 - D_d^3)}\right), \quad (2a)$$

$$\text{RH}_c = \exp\left(\frac{4M_w\sigma_w}{RT\rho_w} \cdot \frac{1}{D_w} - j_c \cdot \frac{\rho_s M_w}{\rho_w M_s} \cdot \frac{D_d^3}{(D_w^3 - D_d^3)}\right), \quad (2b)$$

$$0 = -\frac{4M_w\sigma_w}{RT\rho_w} \cdot \frac{1}{D_w^2} + 3D_w^2 \cdot j_c \cdot \frac{\rho_s M_w}{\rho_w M_s} \cdot \frac{D_d^3}{(D_w^3 - D_d^3)^2}. \quad (2c)$$

[27] Equations (3a)–(3c) is the working Köhler model applied in our analysis of the coated soot particles; these are analogous to equations (2a)–(2c) but contain the particles’ hygroscopic volume fraction ( $\varepsilon$ ). Throughout our analysis, equations (3a)–(3c) will contain the same tuning parameters as in equations (2a)–(2c).

$$\text{RH} = \exp\left(\frac{4M_w\sigma_w}{RT\rho_w} \cdot \frac{1}{D_w} - \varepsilon \cdot j_e \cdot \frac{\rho_s M_w}{\rho_w M_s} \cdot \frac{D_d^3}{(D_w^3 - D_d^3)}\right), \quad (3a)$$

$$\text{RH}_c = \exp\left(\frac{4M_w\sigma_w}{RT\rho_w} \cdot \frac{1}{D_w} - \varepsilon \cdot j_c \cdot \frac{\rho_s M_w}{\rho_w M_s} \cdot \frac{D_d^3}{(D_w^3 - D_d^3)}\right), \quad (3b)$$

$$0 = -\frac{4M_w\sigma_w}{RT\rho_w} \cdot \frac{1}{D_w^2} + 3D_w^2 \cdot \varepsilon \cdot j_c \cdot \frac{\rho_s M_w}{\rho_w M_s} \cdot \frac{D_d^3}{(D_w^3 - D_d^3)^2}. \quad (3c)$$

[28] The two terms on the right side of equations (2a), (2b), (3a) and (3b) are representations of the Kelvin and solute effects. It is recalled that the product of these two phenomenon give rise to the Köhler curve [*Seinfeld and Pandis*, 1998]. Equations (2a), (2b), (3a) and (3b) are developed in Appendix A.

[29] In the working Köhler model (equations (2a), (2b), (2c), (3a), (3b) and (3c)) the quantity  $\rho_s$  is the bulk density of the pure solute,  $\sigma_w$  is the air/water surface tension and  $\rho_w$  is the density of water. For our application of the working Köhler model we take  $\rho_s = 1769 \text{ kg/m}^3$  for ammonium sulfate and  $\rho_s = 1618 \text{ kg/m}^3$  for levoglucosan [*Park et al.*, 1971]. Furthermore, we assume the temperature is a constant ( $T = 298.15 \text{ K}$ ), and we assume constant values for the surface tension ( $\sigma_w = 0.0722 \text{ N/m}$  at  $T = 298.15 \text{ K}$  [*Pruppacher and Klett*, 1997]) and the water density ( $\rho_w = 997 \text{ kg/m}^3$ ).

[30] Figures 3a–3d compare the exact and working Köhler model predictions for pure particles containing either ammonium sulfate or levoglucosan. The basis for the comparisons are ratios formed by dividing the difference between predictions of the working and exact models by the prediction of the exact model. We refer to these ratios as relative departures. Plotted in Figures 3a and 3b is the relative departure for  $D_w$ , evaluated for both ammonium sulfate and levoglucosan at  $\text{RH} = 0.98$  and formulated as  $10^2 \times$

$(D_{w,W} - D_{w,E})/D_{w,E}$  where the “*W*” and “*E*” subscripts indicate the working and exact models, respectively. In addition, Figures 3c and 3d present the relative departure for  $RH_c$ , evaluated as  $10^4 \times (RH_{c,W} - RH_{c,E})/RH_{c,E}$ . In Figures 3a–3d the middle line corresponds to the parameter ( $j_e$  or  $j_c$ ) which produces the best agreement between the working and exact models over the range of dry diameters employed during LExNo. Below and above this line are departure curves obtained using tuning parameters 5% larger and 5% smaller than the optimum value. In section 6.4 we will demonstrate that a relative accuracy of  $\pm 5\%$ , in the case of an instrument-defined tuning parameter, is impossible to achieve experimentally.

#### 4.2. Quantities Derived Via the Working Model

[31] Our application of the working Köhler model is varied. We use CCN measurements and equations (2b) and (2c) to establish the chamber supersaturation calibration (section 3.2), to evaluate the degree to which the CCN instruments broaden the aerosol size distribution (section 6.3), and to derive an instrument-defined value of  $j_c$  and to evaluate its sensitivity to experimental error in  $D_d$  and  $RH_c$  (sections 6.4 and 6.5). Using HHTDMA measurements, and equation (2a), we derive an instrument-defined value of  $j_e$  and assess its sensitivity to experimental error in  $D_d$  and  $RH$  (sections 6.4 and 6.5). Also using HHTDMA measurements, but this time inputted to equations (2b) and (2c), we derive HHTDMA-based critical supersaturations (section 6.5). The final application of the working model is in section 6.6 where we employ equations (3b) and (3c) to derive a CCN-based determination of  $\varepsilon$  (section 6.6) and equation (3a) to derive a HHTDMA-based determination of  $\varepsilon$  (section 6.6). For solving the working model equations we employ an equation solver called “Newton” (IDL, ITT Visual Information Solutions, Boulder, Colorado, USA).

#### 4.3. Validation of the Working Model

[32] The levoglucosan working model was used to derive a  $SS_c$  which was compared to the  $D_d = 100$  nm calculation of *Svenningsson et al.* [2006, Figure 5a]. For ammonium sulfate particles, in the size range of  $40 \text{ nm} < D_d < 90 \text{ nm}$ , predictions of the working model were compared to predictions of the AP3 reference model of *Rose et al.* [2008] which is based on the Aerosol Inorganics Model [*Clegg et al.*, 1998a, 1998b] (<http://www.atmos-chem-phys.net/8/1153/2008/acp-8-1153-2008-supplement.zip>). In both of these comparisons the agreement with the published  $SS_c$  was within  $\pm 0.01$   $SS_c$  units.

#### 4.4. Relations Among $j$ , $\varepsilon$ , $\rho_{ion}$ , and $\kappa$

[33] For our two applications (particle hygroscopicity at  $RH = 0.98$  and particle activation) the droplet solution is expected to be sufficiently dilute for the tuning parameter to be viewed as equivalent to a Van’t Hoff factor. Although approximate, and unessential for our analysis, we view this equivalence as advantageous since many in the aerosol physics and cloud physics communities are familiar with the Van’t Hoff factor and how it varies with solute type and solution strength. In addition to this familiarity, and the model accuracy demonstrated in section 4.3, the working model can be solved forward and backward without recourse to a lookup table or to curve fitting. This facilitates

our analysis of the LExNo data set and is common to other single-parameter water activity formulations [*Fitzgerald et al.*, 1982; *Hudson and Da*, 1996; *Rissler et al.*, 2006; *Petters and Kreidenweis*, 2007; *Wex et al.*, 2007; *Hudson*, 2007].

[34] In this section, we relate the working model to recent theory-based developments. The path leading to the working model equations can be found in Appendix A. We note that the mathematical form of equation (A9) is similar to that developed by *Wex et al.* [2007]. It follows that the hygroscopicity parameter of *Wex et al.* ( $\rho_{ion}$ , their equation (2)) can be expressed in terms of  $j$  and  $\varepsilon$  without recourse to approximation,

$$\rho_{ion} = \varepsilon \cdot j \cdot \frac{\rho_s}{M_s}. \quad (4a)$$

[35] Further, *Wex et al.* [2009] show that for situations germane to our analysis ( $RH \geq 0.98$ ) the hygroscopicity parameter derived by *Petters and Kreidenweis* [2007], and symbolized as  $\kappa$ , is proportional to  $\rho_{ion}$ ,

$$\rho_{ion} = \kappa \cdot \frac{\rho_w}{M_w}. \quad (4b)$$

We present equations (4a) and (4b) for those unfamiliar with recent developments in the application of Köhler theory and to also illustrate how the  $\varepsilon$  derived in this study, and the tuning parameters ( $j_e$  and  $j_c$ ), can be input into the Köhler models of *Wex et al.* [2007] and *Petters and Kreidenweis* [2007].

#### 4.5. Particle Temperature

[36] Because particle temperature is expected to be different in the instruments which cool the aerosol (Laramie, Copenhagen and Leipzig), as opposed to those which warm it (Mainz), and since  $SS_c$  varies with particle temperature via the temperature dependence of the Kelvin effect, the manner in which we apply Köhler theory could lead to substantial interinstrument bias. Here we estimate the magnitude of that bias. The presentation of chamber temperatures shown in Table 1 reveals values between  $13^\circ$  and  $29^\circ\text{C}$  for the upper halves of the Leipzig and Mainz flow tubes, respectively. As we discussed, it is the upper half of these tubes where the maximum chamber supersaturation is established. Table 1 shows that the relevant temperature for the static diffusion instruments, halfway between the two plates, is  $17^\circ\text{C}$ . By exercising the working model with a surface tension derived from a temperature-dependent parameterization for pure water from *Pruppacher and Klett* [1997], and by also accounting for the explicit temperature dependence seen in equations (2b) and (2c), we evaluated  $SS_c$  at both  $13^\circ$  and  $29^\circ\text{C}$ . For the range of dry ammonium sulfate diameters employed ( $35 \text{ nm} \leq D_d \leq 95 \text{ nm}$ ) the absolute bias is no larger than  $0.1$   $SS_c$  units and is a maximum at the smallest dry particle size. In comparison to the maximum difference seen in Figure 3c, resulting from a 5% variation in  $j_c$ , the sensitivity of the modeled  $SS_c$  to temperature is a factor of 2.5 larger. Accounting for the latter sensitivity will require improved characterization of the thermodynamic state within CCN chambers, accurate descriptions of the temperature dependence of both surface tension and water activity, and

models which couple these phenomena. Since this capability is currently lacking, we apply a single temperature (25°C or 298.15 K) in the working Köhler model.

#### 4.6. Particle Shape and Porosity

[37] Difference between the mass-equivalent and mobility-equivalent diameter arises due to particle asphericity and particle porosity. Strictly speaking, the former diameter should be applied in the Köhler model, but for pragmatic reasons we substituted the latter (a measurement) for  $D_d$  in the working Köhler model. Because of this, and since departure from sphericity and compactness is significant for certain types of laboratory-synthesized particles [Kelly and McMurry, 1992], it is important to recognize how these departures alter the calibration of the CCN instruments. The chamber calibrations presented in section 5 employed dried and size-selected ammonium sulfate particles. Prior work indicates that these particles are spherical and compact, at least to the degree necessary for our specific application [Snider et al., 2006]. It follows that the mass-equivalent diameter, for ammonium sulfate particles, can be taken to be the mobility-equivalent diameter. Results presented by Kiselev et al. [2010] demonstrate that the pure levoglucosan particles were compact single-component spheres and again the equivalence between the mobility-equivalent and mass-equivalent diameters is justified. This is not the case for the soot-ammonium sulfate and soot-levoglucosan particles which are revealed to be both aspherical [Stratmann et al., 2010] and porous [Kiselev et al., 2010]. For those particles we derive CCN- and HHTDMA-based values of the  $\varepsilon$  and CCN- and HHTDMA-based values of  $SS_c$ . These calculations rest on the assumption that the value of  $D_d$ , selected in the second Vienna-type electrostatic classifier, is equal to the particles' mass-equivalent diameter. Since the CCNs and the HHTDMA sampled the aerosol in parallel, subsequent to size selection and dilution (section 3.1), the values of  $SS_c$  (and  $\varepsilon$ ) we report are not expected to be shifted relative to one another by virtue of the coated soot particles' asphericity or porosity.

### 5. Analysis Methods

[38] This section presents the chamber supersaturation calibrations (section 5.1), and how those calibrations were applied in the analysis of data from the Laramie, Copenhagen and Mainz instruments (section 5.2). In section 5.3 we describe how measurements from the Leipzig instrument were analyzed.

#### 5.1. Chamber Supersaturation Calibration and Its Error

[39] Table 3 presents the chamber supersaturation calibrations developed for LExNo, demonstrating how the chamber wall temperature ( $T_w$ ), the flow-parallel chamber wall temperature difference ( $\Delta T$ ), and a temperature-dependent "nominal" chamber supersaturation [Snider et al., 2006] are related to the maximum chamber supersaturation. The latter we view as a property of the CCN chamber, and symbolize it as  $SS$  (the chamber supersaturation), to distinguish it from the particle property  $SS_c$  (the critical supersaturation). To be consistent with how we communicate  $SS_c$ , we express  $SS$  in percent units.

[40] Since each of the participating institutions has access to an electrostatic classifier for preparing calibration particles of known size and composition, the chamber supersaturation calibrations were developed at the investigators' home laboratories. Detailed descriptions of this development are provided by Wex et al. [2006], Rose et al. [2008], and Bilde and Svenningsson [2004] for the Leipzig, Mainz, and Laramie/Copenhagen instruments, respectively. Ammonium sulfate was the material used for the chamber supersaturation calibration studies.

[41] The supersaturation error column of Table 3 presents the precision associated with the chamber supersaturation calibration relationship; here referred to as the "supersaturation error." Evaluation of this error requires repeated measurements at several dry test particle sizes, as described by Wex et al. [2006] and Rose et al. [2008] for the Leipzig and Mainz CCN instruments, respectively. For the Laramie and Copenhagen instruments the supersaturation error was derived via an analysis of the linear relationship between  $SS_c$  and the nominal supersaturation [Snider et al., 2006].

[42] At  $SS = 0.5\%$ , a value representative of the LExNo work, the supersaturation error is largest for the Copenhagen instrument ( $\delta_{SS} = 0.09$ ) and smallest for the Mainz instrument ( $\delta_{SS} = 0.02$ ). The supersaturation error for the Copenhagen instrument reflects a difference between chamber calibrations conducted in Leipzig, four days prior to LExNo, and those from the home laboratory. If we eliminate those four data point from the analysis, out of a total of 17 with most from the home laboratory, and use the remaining chamber calibration data points to evaluate the supersaturation error, Copenhagen's  $\delta_{SS}$  is comparable to that for the Laramie instrument (i.e.,  $\delta_{SS} = 0.03$  at  $SS = 0.5\%$ ).

#### 5.2. Laramie, Copenhagen, and Mainz Determination of $SS_c$

[43] In the case of the Laramie, Copenhagen and Mainz instruments the evaluation of activation requires paired determinations of the concentration of particles activating to form cloud droplets (symbolized as CCN) and of the total particle concentration entering the chamber (CN; see section 3.1). Further, these simultaneous concentration measurements must be acquired over a range of supersaturations extending from negligible to complete activation. We define the ratio of the paired CCN and CN concentrations as the active fraction and symbolize it by " $A$ ." As an example, in Figure 4 (top) we plot averages of " $A$ " from the Laramie instrument. These averages are spaced by a 0.02%  $SS$  increment and are overlain by an error limit corresponding the standard deviation of the average. Calculation of an average and standard deviation is possible because the Laramie instrument samples once every 30 s [Snider et al., 2006], yielding 120 individual active fraction measurements over the 1 h duration of a LExNo experiment (section 3.4). Hence, each of the averages is computed from at least ten individual active fraction measurements.

[44] Figure 4 reveals two active fraction plateaus; a minor plateau at  $A \sim 0.3$  and a major plateau at  $A \sim 1$ . In the following paragraph we explain this behavior and how we account for it in analyses of the LExNo data set. Since our analysis departs from that employed by other investigators who, like us, varied  $SS$  while holding the particle size

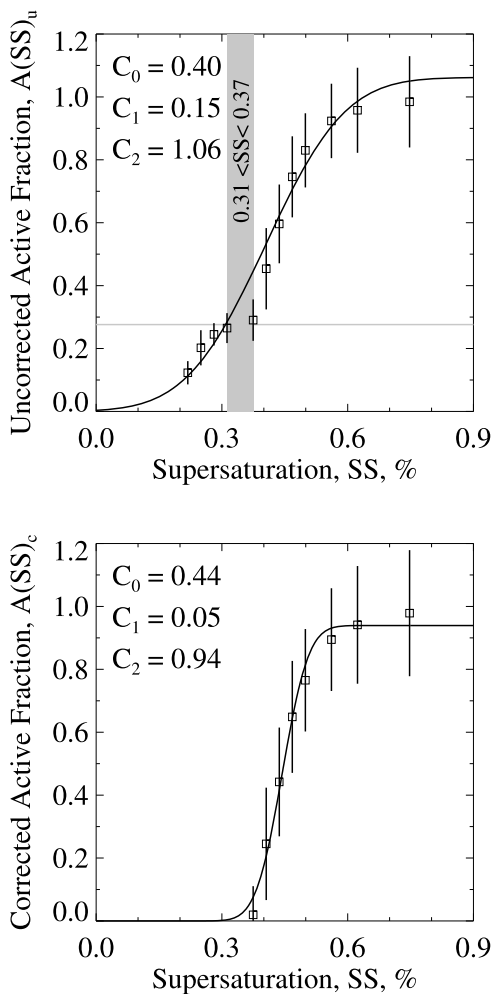


**Figure 4.** (top) Uncorrected active fraction plotted versus supersaturation and (bottom) corrected active fraction versus supersaturation. Data are from the Laramie instrument, LExNo experiment 55. The test particles are composed of pure levoglucosan.

constant [Rosenørn *et al.*, 2006; Sullivan *et al.*, 2009] we describe our method in detail.

[45] The aerosols studied during LExNo were selected from two particle generation systems, both of which produced a relatively broad size distribution (section 3.1) [see also Stratmann *et al.*, 2010, Figure 3]. Of those particles which were selected from this initial size distribution, a subset had larger size, by virtue of the fact that they were transmitted by an electrostatic classifier while carrying two, or more, units of electrical charge. Because these larger particles activate at a lower supersaturation, their presence obscures the activation behavior of the physically smaller, but more numerous, unit charge particles. Accounting for this is a three-step process. First, a value of the supersaturation is identified at the right edge of the minor plateau; we refer to this as  $SS^*$ . Second, individual active fraction values that plot in an interval, extending from  $SS = SS^*$  down to  $SS = SS^* - \Delta SS$ , are averaged to obtain a value for the active fraction representative of the minor plateau region. Figure 4 (top) shows the supersaturation averaging interval as a vertical gray rectangle with width  $\Delta SS = 0.06\%$ .

Third, the average ( $\bar{A}$ , shown as a gray horizontal line) is used to correct the active fraction values in the following manner:

$$A(SS)_c = \frac{A(SS)_u - \bar{A}}{1 - \bar{A}}. \quad (5)$$

Here,  $A(SS)_c$  is the corrected active fraction and  $A(SS)_u$  is the uncorrected active fraction. In section 6.2, where we show more examples of active fraction plotted versus supersaturation we will only show the  $A(SS)_c$  values and we will refer to this as the “active fraction.” Finally, we note that values of  $A(SS)_c$  that correspond to the minor plateau are negative; these values were set to zero for the curve fitting (discussed below) and for the later presentations.

[46] We chose a cumulative Gaussian function to fit the  $A(SS)_c/SS$  data pairs

$$A(SS)_{\text{fit}} = \frac{C_2}{C_1 \cdot \sqrt{2} \cdot \pi} \cdot \int_{-\infty}^{SS} \exp\left(-\left(SS' - C_0\right)^2 / (2 \cdot C_1^2)\right) \cdot d(SS'). \quad (6)$$

Here  $C_2$  is a scaling factor,  $C_1$  is the standard deviation of the Gaussian function and  $C_0$  defines the point where the function is equal to half its maximum value. For the Laramie, Copenhagen and Mainz instruments, we take the value of  $C_0$  to be the critical supersaturation of the test aerosol.

[47] A fit of the corrected active fractions is shown in Figure 4 (bottom), and for contrast, the fit of the uncorrected active fraction values is shown in Figure 4 (top). From an examination of these fit lines, and a comparison of the  $C_1$  values, it is apparent that the unit charge particles (Figure 4, bottom) were distributed more narrowly than indicated by the fit of both charge categories (Figure 4, top). The correction described here was applied to all LExNo experiments that exhibited a substantial minor plateau.

[48] In summation, we analyze a property of the LExNo aerosols, the critical supersaturations ( $SS_c$ ), derived from measurements of active fraction reported by the Laramie, Copenhagen and Mainz instruments. The value of  $SS_c$  comes from a curve fit of the  $A(SS)_c/SS$  data pairs. Also derived is the width of the fitting function ( $C_1$ ).

### 5.3. Leipzig Determination of $SS_c$

[49] The determination of the  $SS_c$  by the Leipzig instrument is based on optical measurements of the wet particle diameter ( $D_w$ ), made at the exit of the flow tube, simultaneous with the recording of the chamber’s wall temperature ( $T_w$ ) [Kiselev *et al.*, 2005; Wex *et al.*, 2006]. More detail on why  $T_w$  controls the supersaturation maximum achieved along the flow tube centerline can be found in section 2 and in work by Wex *et al.* [2006]. The particular  $T_w$  that is observed in association with activation (i.e., with  $D_w$  increasing markedly with increasing  $T_w$ ) was translated to a critical supersaturation via the calibration in Table 3.

## 6. Analysis of the LExNo Data Set

[50] In this section we apply the calibrations and analysis tools, developed in sections 4 and 5, to the CCN and

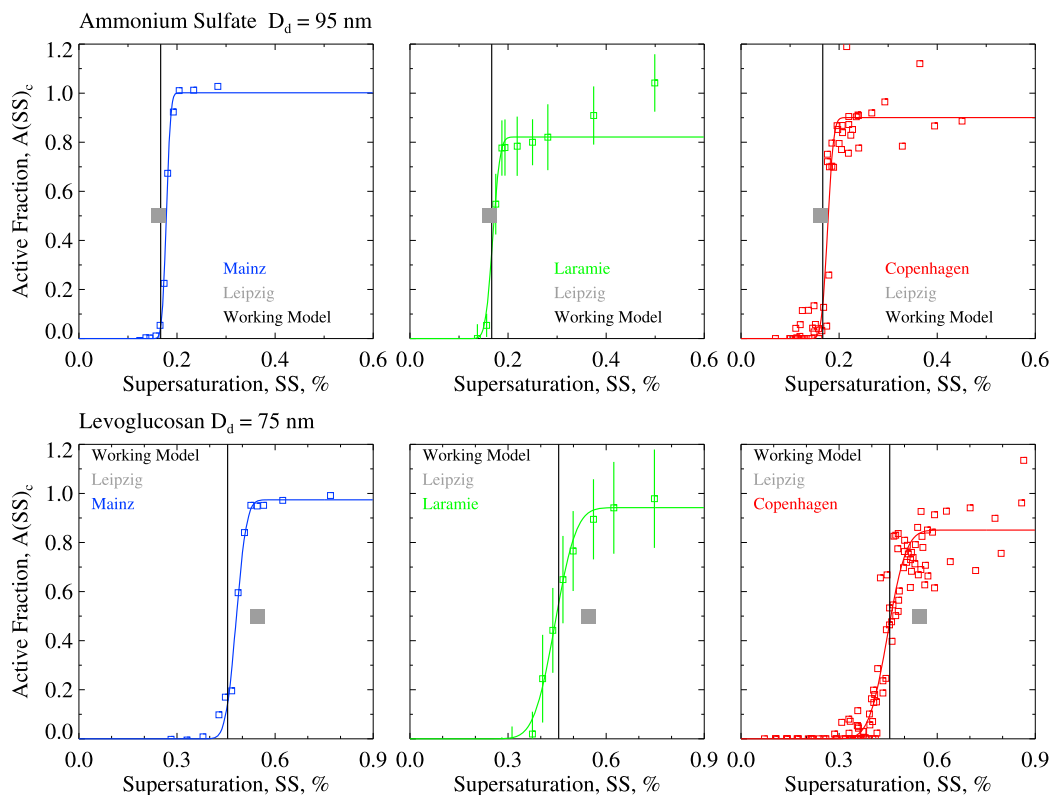


**Figure 5.** Active fraction versus supersaturation: (top) 95 nm diameter ammonium sulfate particles synthesized by spray atomization and (bottom) 75 nm diameter levoglucosan particles synthesized by spray atomization. The  $SS_c$  from the Leipzig instrument is plotted at an active fraction equal to 0.5.

HHTDMA measurements performed during LEXNo. While our main focus is on aerosols synthesized to mimic those produced by combustion, we first evaluate experiments which considered pure ammonium sulfate and pure levoglucosan aerosols.

### 6.1. Pure Solute Aerosols

[51] The dry diameters examined in these experiments were 35, 50, 75 and 95 nm (pure ammonium sulfate) and 50, 75 and 95 nm (pure levoglucosan). In sections 6.2 and 6.3 we present active fractions and  $SS_c$  values for these aerosols and also examine how well the Laramie, Copenhagen and Mainz instruments capture the width of the test particle size distribution function.

### 6.2. Cumulative Activation Spectra

[52] Values of the active fraction are plotted versus supersaturation in Figure 5. The coordinates of this presentation are discussed in sections 5.1 and 5.2. In the case of the Leipzig values, only one of the coordinate axes is relevant to determinations of the  $SS_c$  coming from that instrument (section 5.3), so we plot that particular  $SS_c$  value at an active fraction equal to 0.5. Each of the Laramie data points (Figure 5) is an average of at least ten active fraction values, and as in Figure 4, error bars extend from the average plus 1 standard deviation to the average minus 1 standard deviation. The Copenhagen points are not averaged and these are spaced by a  $SS$  increment smaller than that of the Laramie Mainz. Finally, the Mainz points are averages [Rose *et al.*,

2008]. The larger variability seen in the Copenhagen active fraction values, reflects the fact that those are not averages, and the fact that the effective sample volume of the Mainz instrument is 160 times that of the Copenhagen (and Laramie) instruments.

[53] Figure 5 reveals three significant results of the LEXNo CCN measurements. First, Figure 5 (top) shows that the working model, initialized with the mobility-selected dry particle diameter, produces a  $SS_c$  consistent with the CCN measurements. Second, Figure 5 (top) also show excellent agreement among the four assessments of the  $SS_c$ . Table 2 presents the intraexperiment  $SS_c$  dispersions, defined as the ratio of the intraexperiment standard deviation to the mean ( $\sigma/\langle SS_c \rangle$ ). It is apparent that the  $SS_c$  dispersions are typically 0.02 for the pure ammonium sulfate experiments. The reader is reminded that ammonium sulfate was the material used in the home laboratories to establish the chamber supersaturation calibrations. Third, poorer  $SS_c$  agreement is seen in Figure 5 (bottom) with the Mainz and Leipzig values plotting noticeably larger than either the working model or the Laramie or Copenhagen values. This inconsistency is also reflected in the larger  $SS_c$  dispersions reported for the pure levoglucosan experiments (Table 2).

### 6.3. Broadening of the Particle Size Distribution

[54] Careful examination of Figure 5, for example a comparison of the fit lines shown in the bottom left and bottom middle plots suggests that the slope of the best fit line at active fraction = 0.5 is shallower for the Laramie instrument than it is for the Mainz instrument. This could

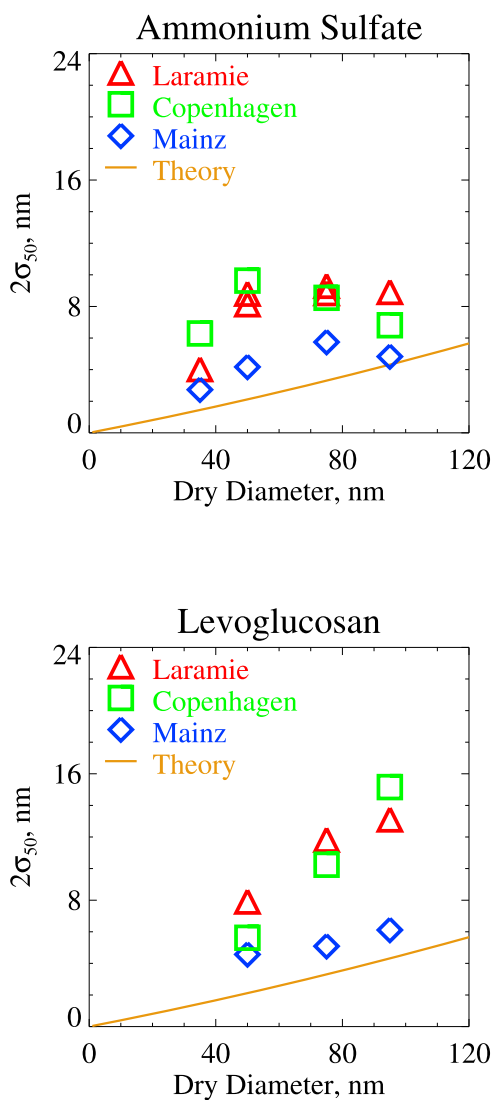


**Figure 6.** The width of the test particle size distribution derived from CCN measurements of the active fraction. Values of  $2\sigma_{50}$  are evaluated as the difference between dry diameters predicted by the working model initialized with  $C_0 - C_1$  and  $C_0 + C_1$  (section 5.2). The theoretical curve is based on work by *Knutson and Whitby* [1975] and corresponds to aerosol-to-sheath flow rate ratio used during LExNo (1-to-10), a mean free path for air (65.1 nm) and a Cunningham slip correction factor [*Seinfeld and Pandis*, 1998, equation (8.34)].

mean that the former is broadening the test aerosol size distribution to a greater degree than the latter. Figure 6 addresses this hypothesis by plotting a derived size distribution width, based on fits of the active fraction data (equation (6)), versus the dry particle diameter for both ammonium sulfate (Figure 6, top) and levoglucosan (Figure 6, bottom). The size distribution widths ( $2\sigma_{50}$ ) were evaluated as the difference between dry diameters predicted by the coupled equations (2b)–(2c) initialized with either  $C_0 - C_1$  or  $C_0 + C_1$  (section 5.2). This calculation mimics the assessment of size distribution broadening previously reported for the Wyoming-type instrument operated by the Laramie group

during LExNo [see *Snider et al.*, 2006, Figure 10]. We conclude that the width of the size distribution, derived from measurements made by two Wyoming-type instruments during LExNo, is approximately 2.5 times the theoretical expectation. For the latter, we assume idealized performance of the Vienna-type electrostatic classifier [*Knutson and Whitby*, 1975], an aerosol-to-sheath flow rate ratio (1-to-10; section 3.1), a mean free path for air (65.1 nm) and a formulation for the Cunningham slip correction factor [*Seinfeld and Pandis*, 1998, equation (8.34)]. From the previous work [*Snider et al.*, 2006], the difference between the Mainz and Wyoming-type instruments seen in Figure 6 is expected, but we are unable to explain it mechanistically. We believe that a factor contributing to the difference is that the Mainz instrument employs an optical particle counter to discriminate and count activated particles [*Roberts and Nenes*, 2005] while the Wyoming-type instruments rely on scattering from an ensemble of particles (activated and unactivated) to infer the activated particle concentration [*Gras*, 1995; *Delene and Deshler*, 2000; *Snider et al.*, 2006].

#### 6.4. Instrument-Defined Values of $j_c$ and $j_e$ : Pure Ammonium Sulfate Particles

[55] Here we demonstrate how the working model, combined with measurements from the CCN instruments, and the HHTDMA, can be used to derive instrument-defined values of  $j_c$  or  $j_e$  for size-selected pure ammonium sulfate particles. The analysis uses an HHTDMA measurement from prior to LExNo [*Hennig et al.*, 2005] (see the final row of their Table 2), and in addition, the average of  $SS_c$  values reported by the Laramie, Copenhagen and Leipzig instruments from LExNo experiment 45. The Mainz instrument did not participate in this experiment (Table 2).

[56] In this section we also gauge consistency between the model tuning parameter and the instrument-defined value and how experimental error in  $D_d$ ,  $SS_c$  and  $RH$  propagates into the instrument-defined value. An experimental error for  $D_d$  is taken from *Snider et al.* [2006] with the upper limit and lower limit set to  $D_d \cdot 1.04$  and  $D_d \cdot 0.96$ , respectively. For the  $SS_c$  error we use  $\pm 0.02 SS_c$  (section 6.2). For the error in the fractional  $RH$  we apply the uncertainty reported by *Hennig et al.* [2005]; i.e.,  $RH - 0.012$  to  $RH + 0.012$ .

[57] Figure 7 presents the instrument-defined values of  $j_c$  and  $j_e$  (indicated by the two crosses), derived by solving equations (2b) and (2c) with measurements of  $SS_c$  and  $D_d$ , and by solving equation (2a) with measurements of  $D_d$ ,  $RH$  and  $D_w$ . A set of four points surrounding the nominal value is also evident. The coordinates of the four points were evaluated by solving for the “ $j$ ” predicted by the working model when initialized with the perturbed measurements shown at each of the four vertices. We view the area of the resulting trapezoid as a domain that encompasses the likely occurrence of the instrument-defined  $j$  values.

[58] From Figure 7 it is apparent that the model tuning parameters  $j_c = 2.40$  and  $j_e = 1.87$  lie within the error trapezoids. Consistent with our definition of the trapezoid we conclude that, within error limits, the instrument-defined  $j$  values (the two crosses) are consistent with the model tuning parameters. Further, we note that the error on the instrument-defined  $j$  exceeds ambiguity in the tuning parameter; recall that the latter is no larger 5% (section 4.1) while the half height of the trapezoids in Figure 7 translate to a 10%

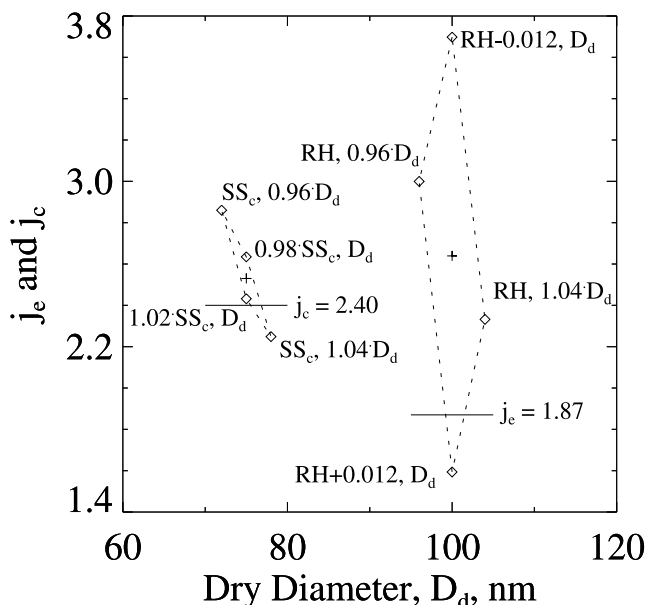


**Figure 7.** On the left of the plot is an instrument-defined value of  $j_c$  (indicated by the plus), the trapezoid-shaped error region, and the tuned value of  $j_c$ . The instrument-defined value of  $j_c$  is based on the average of  $SS_c$  determinations reported by the Laramie, Copenhagen, and Leipzig instruments (experiment 45). The aerosol is composed of 75 nm ammonium sulfate particles and the Mainz instrument did not participate in this experiment (Table 2). On the right of the plot is an instrument-defined value of  $j_e$  (indicated by the plus), the trapezoid-shaped error region, and the tuned value of  $j_e$ . The instrument-defined value of  $j_e$  is based on the fractional RH (0.977) and wet diameter (279 nm) from Hennig *et al.* [2005] (see the final row of their Table 2). The error in fractional relative humidity is taken from Hennig *et al.* The test aerosol was composed of 100 nm dry diameter ammonium sulfate particles.

error in the instrument-defined  $j_c$  and a 40% error in the instrument-defined  $j_e$ . It is also apparent that the  $\pm 4\%$  error in  $D_d$  and the  $\pm 1.2\%$  error in RH are the limiting uncertainties in determinations of the instrument-defined values of  $j_c$  and  $j_e$ , respectively. Because these uncertainties equate to errors in fractional relative humidity which are approximately two parts in ten thousand, in the case of the CCN-based determination, and approximately one part in one hundred in the case of HHTDMA, we conclude that neither technique can approach the accuracy possible in determinations of water activity made in a modern thermochemical laboratory ( $\sim$ one part in one hundred thousand [e.g., Clegg *et al.*, 1998a]). In spite of this pessimistic view of using either CCN or HHTDMA to probe water activity over droplet solutions, via determination of an instrument-defined  $j$ , we do demonstrate that consistent values for the coated soot particles' hygroscopic volume fraction can be derived using these two techniques (section 6.6).

### 6.5. Instrument-Defined $j_c$ and $j_e$ Values: Pure Levoglucosan Particles

[59] In these experiments we examined pure levoglucosan particles prepared at the diameters 50, 75 and 95 nm. As just described we supplement the CCN-based assessments of the  $SS_c$  with measurements from the HHTDMA; the latter is used to derive the instrument-defined  $j_e$  at RH = 0.98. Two additional properties were derived. First, a data set consisting of  $D_d$  and the instrument-defined  $j_e$ , and the working model (equations (2b) and (2c) with the instrument-defined  $j_e$  substituted for  $j_c$ ) were used to evaluate a  $SS_c$  corresponding to the HHTDMA measurements. Second, a data set of  $D_d$  and the CCN-based  $SS_c$ , and the working model (equations (2b) and (2c)) were used to derive the instrument-defined  $j_c$ . Results are shown in Figure 8a, which has no assessment of the  $SS_c$  error limits, and in Figure 8b which shows the instrument-defined values of  $j_e$  and  $j_c$ , and error trapezoids overlain on the Leipzig, Mainz and Laramie determinations of the  $j_c$ . For clarity the error trapezoid is not

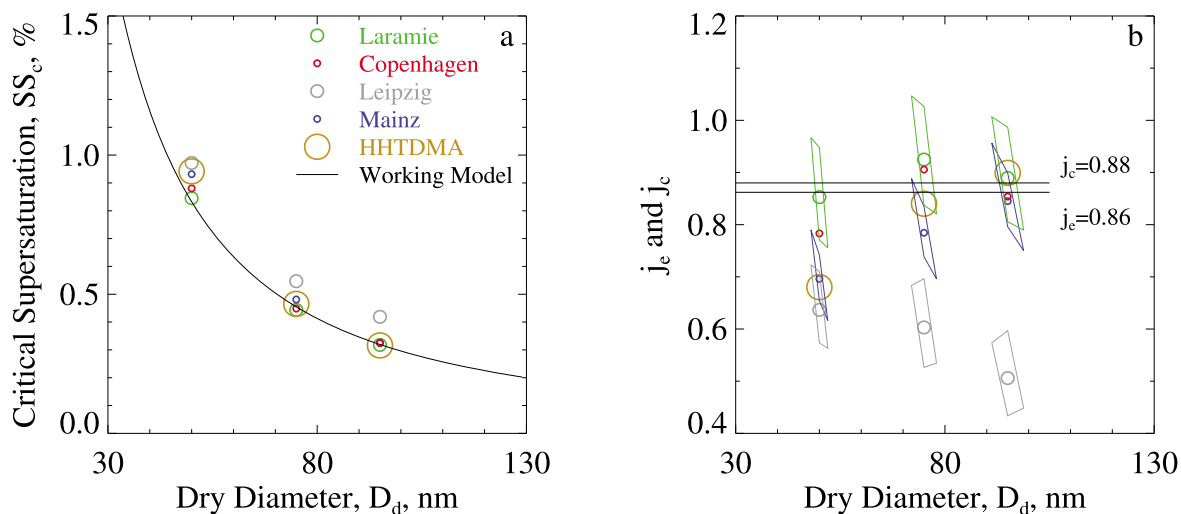


**Figure 8.** (a) Critical supersaturation values based on both CCN and HHTDMA measurements of pure levoglucosan particles. (b) Instrument-defined values of  $j_c$  and  $j_e$ , the trapezoid-shaped error region for the Leipzig, Mainz, and Laramie instruments, and horizontal lines showing the tuned values  $j_c$  and  $j_e$ .

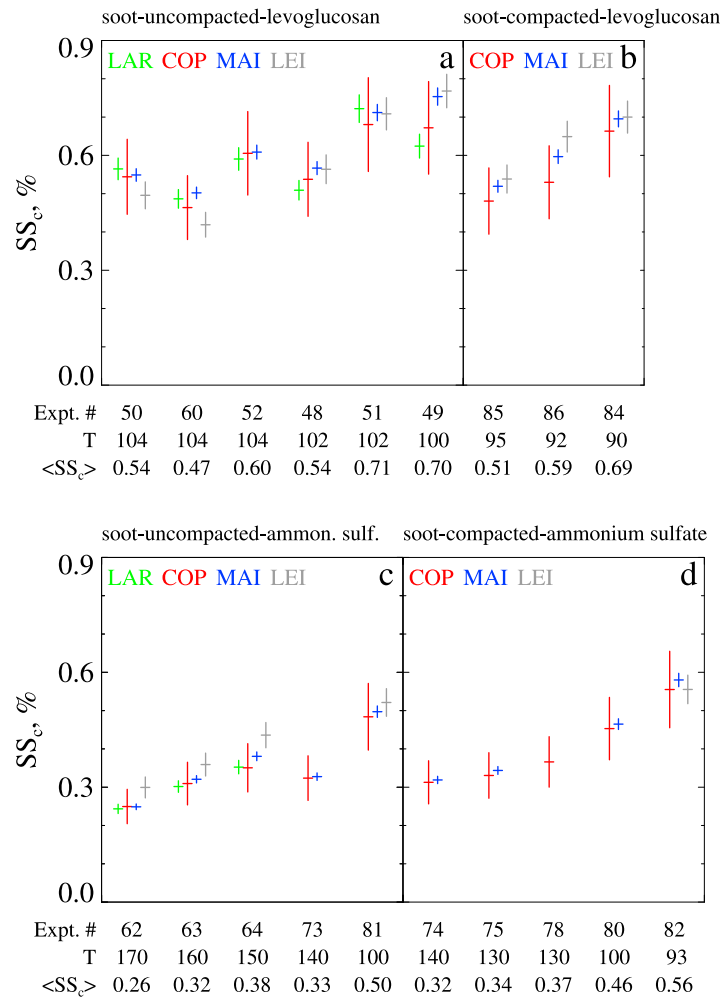


**Figure 9.** Critical supersaturation values, from CCN measurements, and error limits for soot-ammonium sulfate and soot-levoglucosan aerosols. Above each plot is an indication of whether or not the soot particles were treated in the propanol compaction step (section 3.1). Below each plot is the experiment number, the temperature of the oven, and the experiment-averaged  $SS_c$  symbolized as  $\langle SS_c \rangle$ . Within each of the four plots, results are stratified from the highest to the lowest oven temperature. LAR, Laramie static diffusion; COP, Copenhagen static diffusion; MAI, Mainz continuous flow; LEI, Leipzig continuous flow.

shown on values from the Copenhagen and HHTDMA instruments, however, based on our definition of the trapezoid (section 6.4) these data points are indistinguishable from the model tuning parameters.

[60] The  $SS_c$  overpredictions in Figure 8a (Leipzig and Mainz instruments) are seen to translate to an underprediction of  $j_c$  in Figure 8b. It is apparent that the discrepancy between the Leipzig  $j_c$  value and the working model cannot be explained in terms of measurement error in either in  $D_d$  or  $SS_c$  and that this is true for all three  $D_d$  values. Also, the extent of the error trapezoid on the Mainz-based  $j_c$  demonstrates that the low value of  $j_c$  derived for that instrument at  $D_d = 50$  nm cannot be explained in terms of error in  $D_d$  or  $SS_c$ .

## 6.6. Coated Soot Aerosols

[61] The techniques developed for synthesizing coated soot particles, containing soot and hygroscopic material

(ammonium sulfate or levoglucosan) are described in section 3.1. This section evaluates the  $SS_c$  of those particles (Figure 9) and also compares CCN- and HHTDMA-based values of the hygroscopic volume fractions ( $\epsilon$ ) (Figure 10). The CCN-based determinations of  $\epsilon$  came from equations (3b) and (3c) initialized with an experiment-averaged  $SS_c$  ( $\langle SS_c \rangle$ ); results are shown as blue crosses in Figure 10 and more detail about the calculation of both the CCN- and HHTDMA-based determinations of  $\epsilon$  is given below. The Figures 9 and 10 are organized in the same manner, with plots for the four particle types, each with experiment number, the temperature of the levoglucosan or the ammonium sulfate oven and the experiment-averaged  $SS_c$  shown on the abscissa. Results are ranked by oven temperature, decreasing from left to right.

[62] From Figure 10 it is apparent that  $\epsilon$  correlates positively with oven temperature. The temperature dependence stems from the fact that the saturation vapor densities of

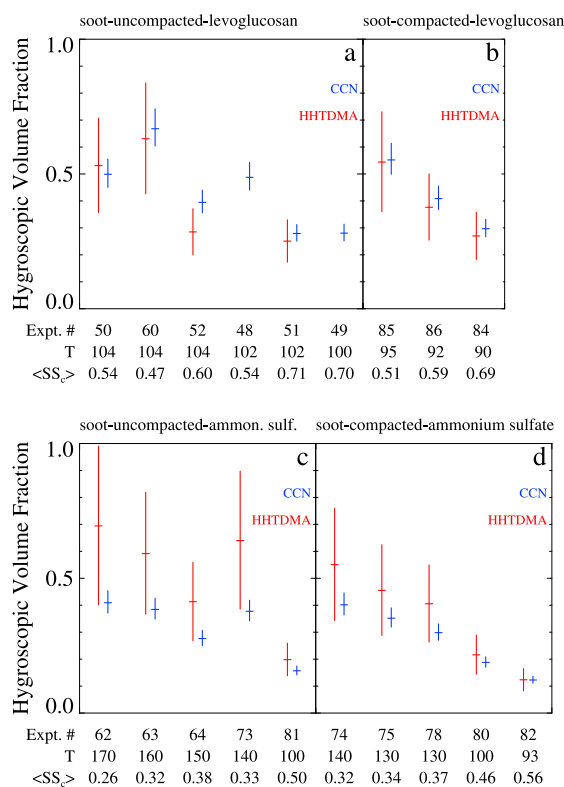


**Figure 10.** Hygroscopic volume fractions for soot-ammonium sulfate and soot-levoglucosan aerosols, derived from both CCN and HHTDMA measurements. Above each plot is an indication of whether or not the soot particles were treated in the propanol compaction step (section 3.1). Below each plot is the experiment number, the temperature of the oven, and the experiment-averaged  $SS_c$ , symbolized as  $\langle SS_c \rangle$ . Within each of the four plots, results are stratified from the highest to the lowest oven temperature. HHTDMA measurements are not available for experiments 48 and 49 (Table 2).

both levoglucosan and ammonium sulfate increase with increasing temperature, resulting in more vapor available for condensation, subsequent to quenching, at larger oven temperatures. This correlation is consistent with prior studies [e.g., Tao and McMurry, 1989] and with the correlation between coating mass and oven temperature presented by Kiselev *et al.* [2010]. Figure 9 shows that  $SS_c$  correlates inversely with oven temperature, consistent with the positive  $\varepsilon$ -temperature correlation (Figure 10), and Köhler theory.

[63] In Figures 9b, 9d, 10b and 10d the modifier “compacted” is used to indicate exposure of the soot particles to an elevated partial pressure of propanol prior to their treatment in the ovens (section 3.1). As was reported previously [Kütz and Schmidt-Ott, 1992], exposure to propanol vapor causes a low density soot particle to restructure into a more compact shape. Figures 9c and 9d indicate comparable values of  $SS_c$  for the same oven temperatures (e.g., 100° and 140°C) and this result is also evident in Figures 10c and 10d, again at 100° and 140°C, where the values of  $\varepsilon$  are seen to be negligibly affected by the propanol compaction step. We conclude that particle restructuring, due to exposure to propanol, had a negligible effect on the amount of con-

densed ammonium sulfate. Khalizov *et al.* [2009] and Pagels *et al.* [2009] report similar results, showing that soot aggregate and polystyrene latex particles, both having the same mobility equivalent diameter and processed similarly, acquire nearly the same mass of sulfuric acid.

[64] The effect of propanol compaction in the soot-levoglucosan experiments is difficult to interpret. First, there is no “compacted” experiment with an oven temperature equal to that in an “uncompacted” experiment. Second, values of  $\varepsilon$  from the compacted experiments are comparable to those from the warmer uncompacted experiments (see Figures 10a and 10b). Henning *et al.* [2010] comment that the temperature and morphology dependence of soot uptake of levoglucosan was confounded by the addition of a fresh batch of levoglucosan to the oven. That change occurred subsequent to the first set of soot-levoglucosan experiments (Figure 10a) and prior to the second set of experiments (Figure 10b). Regrettably, the LExNo data set is incomplete in its assessment of the interaction of soot particles with levoglucosan vapor.

[65] The error limits in Figure 9 correspond to the values of the supersaturation error ( $\delta_{SS}$ ) presented in Table 3. Based on the discussion in section 5.1 we take  $\delta_{SS}$  to be a random error of magnitude equal to 1 standard deviation. Going through Figures 9a, 9b, 9c and 9d one can pick out examples of agreement at 1 standard deviation for experiments 52, 73, 74, 80, and at 2 standard deviations for experiments 50, 51, 75, 81, 84, and 82. It is also noted that three experiments (49, 64 and 86) have a particularly large positive departure for the Leipzig instrument, and that two of these (49 and 86) have a substantial positive departure for the Mainz instrument. These three cases are discussed further in section 7.

[66] In Figure 10 we compare values of  $\varepsilon$  corresponding to both the HHTDMA and CCN measurements. The CCN-based values of  $\varepsilon$  came from equations (3b) and (3c), solved with  $\varepsilon$  and the critical wet diameter as unknowns, subject to the experimental constraints of  $\langle SS_c \rangle$  (the experiment-averaged  $SS_c$ ),  $D_d$ , and with the tuning parameter  $j_c$  and material constants as inputs. The HHTDMA-based values of  $\varepsilon$  came from equation (3a), with  $\varepsilon$  as the unknown, subject to the experimental constraints of  $D_d$ , RH and  $D_w$ , and with the tuning parameter  $j_e$  and material constants as inputs. Overall there is agreement, within experimental error, between the CCN- and HHTDMA-based values of  $\varepsilon$ . Also apparent (Figure 10c) is a systematic difference among the CCN- and HHTDMA-based values of  $\varepsilon$ . The most obvious examples of this are experiments 62, 63 and 73 with  $\varepsilon \sim 0.40$  and  $\varepsilon \sim 0.65$  coming from the CCN and HHTDMA data sets, respectively. Since the LExNo aerosol mass spectrometer measurements show that the end product of the ammonium sulfate condensation step was actually ammonium hydrogen sulfate ( $NH_4HSO_4$ ), not the expected  $(NH_4)_2SO_4$  [Henning *et al.*, 2010], we investigated if the differences seen in Figure 10c could be explained chemically. While it is true that performing the Köhler theory calculation using a water activity basis set for  $NH_4HSO_4$  does decrease the  $\varepsilon$  derived from the HHTDMA measurements, a comparable decrease is also obtained for the CCN-based values of  $\varepsilon$ . Rather than show that result, we draw the reader’s attention to the error limits in Figure 10. For the HHTDMA values the error limits were derived by perturbing the working Köhler model with a

fractional relative humidity above and below the nominal value (section 3.3). The range of this perturbation is from  $RH - 0.012$  to  $RH + 0.012$  [Hennig *et al.*, 2005]. For the CCN data points the perturbation of the experiment-averaged  $SS_c$  is from  $\langle SS_c \rangle - 0.05 \cdot \langle SS_c \rangle$  to  $\langle SS_c \rangle + 0.05 \cdot \langle SS_c \rangle$  and the range of the perturbation was obtained by averaging the  $SS_c$  dispersions (Table 2) over all of the coated soot experiments. With these error limits we see an overlap between the lower limit of the HHTDMA-based  $\varepsilon$  and the value of  $\varepsilon$  derived using  $\langle SS_c \rangle$ . This result reinforces the finding (section 6.4) that the RH measurement uncertainty (approximately one part in a hundred) propagates into a 40% error in parameters which are multiplicative in the exponential representation of the water activity in equation (3a). This point is also emphasized by Petters and Kreidenweis [2007].

## 7. Levoglucosan Particles in the Continuous Flow and Static Diffusion Instruments

[67] Here our focus is on experiments with particles containing levoglucosan, primarily because of past and ongoing efforts aimed at gaining insight into the role of organic aerosol components in cloud droplet nucleation. The reader will recall from section 6.5, and Figures 8a and 8b, that there is a suspicion of significant  $SS_c$  overestimation in one experiment for Mainz and in three experiments for Leipzig. Here we conduct an examination of the  $SS_c$  values shown in Figure 9 and their experimental error. In this discussion the  $D_d$  experimental error, discussed in section 6.5, is ignored because it affects all CCN measurements equally. An examination of the  $SS_c$  values, together with their error limits ( $\delta_{SS}$ , section 6.6), reveals no experiment where a continuous flow instrument departs by greater than 2 standard deviations from the Copenhagen static diffusion instrument. However, if we accept the assertion that the supersaturation error for the Copenhagen instrument is smaller than that reported in Table 3, comparable to that of the Laramie instrument (section 5.1), we detect three experiments where the Leipzig instrument does depart by greater than 2 standard deviations, and positively, from static diffusion CCN measurements (49, 64 and 86). Since the 64 experiment is for soot-ammonium sulfate particles (Figure 9c), it seems imprudent to conclude that the continuous flow  $SS_c$  values are positively biased relative to the static diffusion values only in the soot-levoglucosan experiments.

[68] Figure 2 shows model calculations indicating that the interval of maximum supersaturation exposure is smaller for the continuous flow (Leipzig and Mainz) relative to the static diffusion (Laramie and Copenhagen) instruments. Given this range of exposure times it is plausible that the time required for a particle to achieve its critical size can approach, or exceed, the interval of maximum supersaturation exposure. In that case the particles'  $SS_c$  is overestimated, that is, a larger supersaturation must be applied to increase the growth rate so that the critical size is reached in the time allotted. In spite of the skepticism of the previous paragraph, the results shown in Figures 8a and 8b, plus those in Figure 9 (experiments 49 and 86), hint that the  $SS_c$  of some levoglucosan-containing aerosols were overestimated by the Leipzig and Mainz instruments. We cannot validate this suspicion, but we note that a necessary condition is that water condensation on levoglucosan particles

must be retarded, relative to that on ammonium sulfate particles. We examined the possibility of growth retardation, within the Laramie instrument, by employing the approach of Delene and Deshler [2000]. Based on that analysis, which is presented in the auxiliary material, we did not find any evidence for the retardation of condensational growth on pure levoglucosan particles, relative to that on pure ammonium sulfate particles. This does not preclude the possibility that activation of levoglucosan is kinetically limited, within the continuous flow instruments, but it does establish conditions in a static diffusion instrument where it does not occur. Future laboratory studies should target aerosols composed of material known to limit condensational growth to elucidate the importance of this possible effect.

## 8. Conclusions

[69] LExNo brought together the two most common instruments deployed for CCN measurement. These two instruments, manufactured by the University of Wyoming and Droplet Measurement Technologies, were operated with the Leipzig CCN instrument and the high-humidity tandem differential mobility analyzer. Laboratory investigations of both pure solute and coated soot particles were conducted at the Leipzig facility.

[70] A significant result of LExNo is the level of agreement among the  $SS_c$  values derived from the CCN measurements, from the HHTDMA measurements, and from theory. For the five experiments that examined pure ammonium sulfate particles in the diameter range 35 to 95 nm, excellent agreement is evident from the  $SS_c$  dispersions in Table 2, and in the presentation of one of these experiments in Figure 5 (top). Comparable agreement was found for static diffusion CCN measurements, and the HHTDMA measurements, in the investigations of pure levoglucosan particles (section 6.5). Taken together, these results support the conjecture that levoglucosan solutions, both at  $RH = 0.98$ , and at activation, do not behave ideally. This is consistent with the Zandovskii-Stokes-Robinson calculations reported by Svenningsson *et al.* [2006], but since the upper limit error for the Laramie instrument reaches the value  $j_c = 1$  (Figure 8b) we cannot exclude the possibility of ideal solution behavior. We conclude, like Svenningsson *et al.*, that ideal solution behavior for levoglucosan lies within error limits placed on  $SS_c$  values derived using a static diffusion instrument.

[71] Figure 8 also illustrates a discrepancy among determinations of the  $SS_c$  coming from the static diffusion and continuous flow instruments. If we only had results from the continuous flow instruments we would have concluded that the hygroscopicity of levoglucosan solutions, at criticality, is significantly smaller than anticipated assuming ideal solution behavior. This finding could be explicable in terms of residual water carried by the test particles [Mikhailov *et al.*, 2009], as long as one also discounts consistency among the static diffusion and HHTDMA measurements and the working model (Figure 8). Also, the assertion is not supported by the finding of Kiselev *et al.* [2010] who demonstrated that the effective density of the pure levoglucosan particles was indistinguishable from the intrinsic levoglucosan density ( $1618 \text{ kg/m}^3$  [Park *et al.*, 1971]).

[72] The difference among the static diffusion and continuous flow measurements, in particular at  $D_d = 50 \text{ nm}$

and also at larger values of  $D_d$  for the Leipzig instrument (Figure 8), may be explained by droplet growth retardation. However, we view this as tentative for two reasons: (1) condensational growth kinetics on pure levoglucosan and pure ammonium sulfate particles are comparable in the Laramie instrument (auxiliary material), and (2) the aerosol flow humidification that occurs upstream of the Leipzig flow tube (section 3.1) could have suppressed the kinetically limited deliquescence documented for levoglucosan particles by *Mikhailov et al.* [2009]. Further research is needed to resolve this issue.

[73] By conducting parallel measurements with four CCN instruments, LExNo facilitated an assessment of the intraexperiment  $SS_c$  error (Table 2). Typical errors are  $\pm 0.02 \cdot SS_c$  and  $\pm 0.05 \cdot SS_c$  for experiments with pure ammonium sulfate particles and coated soot particles, respectively. In general, this variability is consistent with supersaturation errors reported by operators of the CCN instruments. Compared to prior CCN intercomparison studies [*Jiusto et al.*, 1981; *Hudson and Alofs*, 1981] the level of agreement obtained during LExNo represents a significant improvement. The latter reference reports on four experiments which investigated pure ammonium sulfate aerosols. In that work the intraexperiment  $SS_c$  dispersions were approximately  $0.08$  ( $40 \text{ nm} \leq D_d \leq 140 \text{ nm}$ ), about a factor of three larger than we obtained during LExNo ( $50 \text{ nm} \leq D_d \leq 95 \text{ nm}$ ; Table 2). Also explored during LExNo was the degree to which CCN instruments broaden the aerosol size distribution. We conclude that there is little evidence for this occurring in the Mainz and that the Wyoming-type instruments (Laramie and Copenhagen) broaden by a factor 2.5 in comparison to the width of the size distribution inferred from electrostatic classifier theory.

[74] Our final two conclusions are cautionary. First, LExNo was designed to maintain the test aerosol population constant for approximately 1 h. It is thus likely that applications which require time resolution better than 1 h will be subject to error larger than we document here. Second, because of limitations in our understanding of how thermodynamic state varies within the CCN instruments, we chose not to account for a bias ( $0.1 SS_c$  units for  $D_d = 35 \text{ nm}$ , section 4.5) resulting from suspected differences in particle temperature among the four CCN instruments. Accounting for this bias should be an objective of further studies.

## Appendix A

[75] Properties of a liquid solution droplet consisting of water, a hygroscopic solute and a water-insoluble component are analyzed. First, the Köhler theory working model is derived, second, we show that the working model's tuning parameter approximates the Van't Hoff factor, and third, we evaluate formulaic error resulting from the working model's simplified description of the water activity.

[76] Water activity for a water/solute solution can be expressed in terms of the mole amounts of water ( $n_w$ ), solute ( $n_s$ ) and the Van't Hoff factor ( $i$ ),

$$a(m) = \frac{n_w}{n_w + i \cdot n_s} = \frac{1}{1 + i \cdot \frac{n_s}{n_w}} = \frac{1}{1 + i \cdot M_w \cdot m}. \quad (\text{A1})$$

Here  $M_w$  is the molecular mass of water and  $m$  is the molality. Empiricism demonstrates that  $i$  is a nonlinear function of  $m$  [see, e.g., *McDonald*, 1953]; this nonlinearity can stifle accurate  $a(m)$  parameterization by approximate forms of the Köhler equation. In the following development the exact and approximate water activities are symbolized as  $a(m)$  and  $a_w$ , respectively.

[77] Assuming water and solute contribute to the solution volume as pure components (volume additivity assumption), and assuming that the dry aerosol particle is spherical and compact, the mole amount of water carried by a solution droplet of diameter  $D_w$  is

$$n_w = \frac{\pi}{6} \cdot \frac{\rho_w}{M_w} \cdot (D_w^3 - D_d^3). \quad (\text{A2})$$

Here  $D_d$  is the diameter of the dry aerosol particle and  $\rho_w$  is the density of liquid water. Evoking the spherical assumption again, the mole amount of the solute is

$$n_s = \varepsilon \cdot \frac{\pi}{6} \cdot \frac{\rho_s}{M_s} \cdot D_d^3, \quad (\text{A3})$$

where  $\varepsilon$  is the dry particles' hygroscopic volume fraction and  $\rho_s$  and  $M_s$  are the density and molecular mass of hygroscopic solute.

[78] The Köhler equation relates the fractional relative humidity over a solution droplet (RH) to the product of water activity and the Kelvin effect. For the latter we assume that the surface tension ( $\sigma_w$ ) is a constant, and solvent/solute volume additivity. The volume additivity assumption allows the water partial specific volume to be equated to  $\rho_w^{-1}$  [*Mita*, 1979]. With these simplifications of the Kelvin effect, the Köhler equation becomes

$$\text{RH} = a(m) \cdot \exp\left(\frac{4M_w\sigma_w}{\rho_w R T D_w}\right). \quad (\text{A4})$$

Here  $R$  is the universal gas constant and  $T$  is absolute temperature.

[79] The combination of equations (A1), (A2), (A3) and (A4) yields the following form of the Köhler equation:

$$\text{RH} = a_w \cdot \exp\left(\frac{4M_w\sigma_w}{\rho_w R T D_w}\right) = \left( \frac{\exp\left(\frac{4M_w\sigma_w}{\rho_w R T D_w}\right)}{1 + \varepsilon \cdot i \cdot \frac{M_w \cdot \rho_s}{M_s \cdot \rho_w} \cdot \frac{D_d^3}{(D_w^3 - D_d^3)}} \right). \quad (\text{A5})$$

[80] The water activity in equation (A5), symbolized by  $a_w$  to distinguish it from the exact water activity ( $a(m)$ , equation (A1)), is approximate because of the volume additivity assumption coming from equation (A2). This intermediate approximation of the water activity is given by equation (A6),

$$a_w = \frac{1}{1 + \varepsilon \cdot i \cdot \frac{M_w \cdot \rho_s}{M_s \cdot \rho_w} \cdot \frac{D_d^3}{(D_w^3 - D_d^3)}}. \quad (\text{A6})$$

The path leading to the working model requires three additional approximations. First, we assume that the second

term in the dominator of equation (A6) is small relative to one, second, we linearize  $a_w$  by Taylor series expansion  $[(1 + x)^{-1} \approx 1 - x]$ ,

$$a_w = 1 - \varepsilon \cdot i \cdot \frac{\rho_s \cdot M_w}{\rho_w \cdot M_s} \cdot \frac{D_d^3}{(D_w^3 - D_d^3)}, \quad (\text{A7})$$

and third, we approximate equation (A7) as an exponential  $[1 - x \approx \exp(-x)]$ . The approximate form of the water activity is

$$a_w = \exp\left(-\varepsilon \cdot i \cdot \frac{\rho_s \cdot M_w}{\rho_w \cdot M_s} \cdot \frac{D_d^3}{(D_w^3 - D_d^3)}\right), \quad (\text{A8})$$

and the Köhler equation becomes

$$\text{RH} = \exp\left(\frac{4M_w\sigma_w}{\rho_w RTD_w} - \varepsilon \cdot i \cdot \frac{\rho_s \cdot M_w}{\rho_w \cdot M_s} \cdot \frac{D_d^3}{(D_w^3 - D_d^3)}\right). \quad (\text{A9})$$

[81] Comparability between equation (A9) and equation (3a) implies that the tuning parameter  $j_e$  approximates  $i$ . Comparability is also seen between equation (A9) and equation (3b), both applied to the critical point. Comparisons can also be made for a particle which does not contain a water-insoluble component; i.e., equation (A9) (with  $\varepsilon = 1$ ) compared to equation (2a), and equation (A9) (with  $\varepsilon = 1$ ) compared to equation (2b). In those two cases, for the situation at  $\text{RH} = 0.98$  and for the situation at the critical point, the tuning parameter is again seen to approximate the Van't Hoff factor. Necessary for the development of equation (A9), and thus for establishing the connection between the tuning parameter and the Van't Hoff factor, is the assumption that the magnitude of the exponentiated term in equation (A8) is small relative to one, and hence, that the solution is relatively dilute.

[82] Here we evaluate differences between equations (A5) and (A9) for dilute, but not infinitely dilute, solution droplets. For this we assume the dry particle is composed of either ammonium sulfate or levoglucosan, and we exercise the models over the range  $35 \text{ nm} \leq D_d \leq 95 \text{ nm}$ . In this analysis we use the water activity basis sets in the exact model (section 4.1) and assume volume additivity. First, we evaluate the molality corresponding to prescribed values ( $D_d$  and  $D_w$ ), second, the water activity (water activity basis sets described in section 4.1), and third, the Van't Hoff factor corresponding to the values of molality and water activity ( $i$ , equation (A1)). The derived values of water activity and  $i$  are applied in equations (A5) and (A9), respectively.

[83] At  $\text{RH} = 0.98$ , and for the case with the largest difference between equations (A5) and (A9) (95 nm dry ammonium sulfate particle), equation (A9) predicts a value of  $D_w$  which is 2.6 nm larger than that predicted by equation (A5). At the critical point, equation (A9) predicts a  $\text{SS}_c$ , which is 0.002  $\text{SS}_c$  units smaller than equation (A5). The latter comparison is for the extreme case of a 35 nm diameter levoglucosan particle. In these comparisons we use the same description of the Kelvin effect, and the same water activity basis set, hence, the differences are solely due to the differing formulations of the water activity in equations (A5) and (A9). The comparisons demonstrate that acceptable model agreement, at least to the degree necessary

for analysis of the LExNo data, can be obtained using equation (A9) with  $i$  replaced by a tuning parameter.

[84] **Acknowledgments.** Several LExNo participants (G. Frank, A. Kiendler-Scharr, A. Kristensson, T. F. Mentel, D. Rose, J. Snider, and S. Walter) thank Atmospheric Composition Change: a European Network (ACCENT) for travel support. M. Bilde thanks the Nordic Center of Excellence, Research Unit BACCI, and Danish Natural Science Research Council for financial support. As a whole, the LExNo group thanks Simon Clegg. LExNo was hosted by the research group in Leipzig; their efforts were essential for bringing the study to fruition. The work of three reviewers is also acknowledged.

## References

- Andreae, M. O., et al. (1988), Biomass-burning emissions and associated haze layers over Amazonia, *J. Geophys. Res.*, *93*(D2), 1509–1527, doi:10.1029/JD093iD02p01509.
- Asa-Awuku, A., G. J. Engelhart, B. H. Lee, S. N. Pandis, and A. Nenes (2009), Relating CCN activity, volatility, and droplet growth kinetics of beta-caryophyllene secondary organic aerosol, *Atmos. Chem. Phys.*, *9*, 795–812.
- Bilde, M., and B. Svenningsson (2004), CCN activation of slightly soluble organics: The importance of small amounts of inorganic salt and particle phase, *Tellus, Ser. B*, *56*, 128–134.
- Boucher, O., and T. L. Anderson (1995), General circulation model assessment of the sensitivity of direct climate forcing by anthropogenic sulfate aerosols to aerosol size and chemistry, *J. Geophys. Res.*, *100*(D12), 26,117–26,134, doi:10.1029/95JD02531.
- Brechtel, F. J., and S. M. Kreidenweis (2000), Predicting particle critical supersaturation from hygroscopic growth measurements in the humidified TDMA, Part I: Theory and sensitivity studies, *J. Atmos. Sci.*, *57*, 1854–1871, doi:10.1175/1520-0469(2000)057<1854:PPCSFH>2.0.CO;2.
- Chuang, P. Y., R. J. Charlson, and J. H. Seinfeld (1997), Kinetic limitations on droplet formation in clouds, *Nature*, *390*, 594–596, doi:10.1038/37576.
- Chýřlek, P., and J. G. D. Wong (1998), Erroneous use of the modified Köhler equation in cloud an aerosol physics applications, *J. Atmos. Sci.*, *55*, 1473–1477, doi:10.1175/1520-0469(1998)055<1473:EUOTMK>2.0.CO;2.
- Clegg, S. L., P. Brimblecombe, and A. S. Wexler (1998a), A thermodynamic model of the system  $\text{H}^+ - \text{NH}_4^+ - \text{SO}_4^{2-} - \text{NO}_3^- - \text{H}_2\text{O}$  at tropospheric temperatures, *J. Phys. Chem. A*, *102*, 2137–2154, doi:10.1021/jp973042r.
- Clegg, S. L., P. Brimblecombe, and A. S. Wexler (1998b), A thermodynamic model of the system  $\text{H}^+ - \text{NH}_4^+ - \text{Na}^+ - \text{SO}_4^{2-} - \text{NO}_3^- - \text{Cl}^- - \text{H}_2\text{O}$  at 298.15 K, *J. Phys. Chem. A*, *102*, 2155–2171, doi:10.1021/jp973043j.
- Delene, D. J., and T. Deshler (2000), Calibration of a photometric cloud condensation nucleus counter designed for deployment on a balloon package, *J. Atmos. Oceanic Technol.*, *17*, 459–467, doi:10.1175/1520-0426(2000)017<0459:COAPCC>2.0.CO;2.
- de Oliveira, J. C. P., and G. Vali (1995), Calibration of a photoelectric cloud condensation nucleus counter, *Atmos. Res.*, *38*, 237–248, doi:10.1016/0169-8095(94)00095-U.
- Fitzgerald, J. W. (1974), The effect of aerosol composition on cloud droplet size distribution: A numerical study, *J. Atmos. Sci.*, *31*, 1358–1367, doi:10.1175/1520-0469(1974)031<1358:EOACOC>2.0.CO;2.
- Fitzgerald, J. W., W. A. Hoppel, and M. A. Vietti (1982), The size and scattering coefficient of urban aerosol particles at Washington, DC as a function of relative humidity, *J. Atmos. Sci.*, *39*, 1838–1852, doi:10.1175/1520-0469(1982)039<1838:TSASCO>2.0.CO;2.
- Gras, J. L. (1995), CN, CCN and particle size in the southern ocean air at Cape Grim, *Atmos. Res.*, *35*, 233–251, doi:10.1016/0169-8095(94)00021-5.
- Hennig, T., A. Massling, F. J. Brechtel, and A. Wiedensohler (2005), A tandem DMA for highly temperature-stabilized hygroscopic particle growth measurements between 90% and 98% relative humidity, *J. Aerosol Sci.*, *36*, 1210–1223, doi:10.1016/j.jaerosci.2005.01.005.
- Henning, S., et al. (2010), Soluble mass, hygroscopic growth and droplet activation of coated soot particles during LACIS Experiment in November (LEXNo), *J. Geophys. Res.*, *115*, D11206, doi:10.1029/2009JD012626.
- Hudson, J. G. (2007), Variability of the relationship between particle size and cloud-nucleating ability, *Geophys. Res. Lett.*, *34*, L08801, doi:10.1029/2006GL028850.
- Hudson, J. G., and D. J. Alofs (1981), Performance of the continuous flow diffusion chambers, *J. Rech. Atmos.*, *15*, 321–331.
- Hudson, J. G., and X. Y. Da (1996), Volatility and size of cloud condensation nuclei, *J. Geophys. Res.*, *101*(D2), 4435–4442, doi:10.1029/95JD00192.

- Jiusto, J. E., R. E. Ruskin, and A. Gagin (1981), CCN comparisons of static diffusion chambers, *J. Rech. Atmos.*, *15*, 291–302.
- Katz, J. L., and P. Mirabel (1975), Calculation of supersaturation profiles in thermal diffusion cloud chambers, *J. Atmos. Sci.*, *32*, 646–652, doi:10.1175/1520-0469(1975)032<0646:COISPIT>2.0.CO;2.
- Kelly, W. P., and P. H. McMurry (1992), Measurement of particle density by inertial classification of differential mobility-generated monodisperse aerosols, *Aerosol Sci. Technol.*, *17*, 199–212, doi:10.1080/02786829208959571.
- Khalizov, A. F., R. Zhang, D. Zhang, H. Xue, J. Pagels, and P. H. McMurry (2009), Formation of highly hygroscopic soot aerosols upon internal mixing with sulfuric acid vapor, *J. Geophys. Res.*, *114*, D05208, doi:10.1029/2008JD010595.
- Kiselev, A., H. Wex, F. Stratmann, A. Nadeev, and D. Karpushenko (2005), White-light optical particle spectrometer for in situ measurement of condensational growth of aerosol particles, *Appl. Opt.*, *44*, 4693–4701, doi:10.1364/AO.44.004693.
- Kiselev, A., C. Wennrich, F. Stratmann, H. Wex, S. Henning, T. F. Mentel, J. Schneider, S. Walter, and I. Lieberwirth (2010), Morphological characterization of soot aerosol particles during LACIS Experiment in November (LExNo), *J. Geophys. Res.*, *115*, D11204, doi:10.1029/2009JD012635.
- Knutson, E. O., and K. T. Whitby (1975), Aerosol classification by electric mobility: Apparatus, theory, and applications, *J. Aerosol Sci.*, *6*, 443–451, doi:10.1016/0021-8502(75)90060-9.
- Kütz, S., and A. Schmidt-Ott (1992), Characterization of agglomerates by condensation-induced restructuring, *J. Aerosol Sci.*, *23*, Suppl. 1, 357–360, doi:10.1016/0021-8502(92)90423-S.
- Lance, S., J. Medina, J. N. Smith, and A. Nenes (2006), Mapping the Operation of the DMT Continuous Flow CCN Counter, *Aerosol Sci. Technol.*, *40*, 242–254, doi:10.1080/02786820500543290.
- Levin, Z., and W. R. Cotton (2009), *Aerosol Pollution Impact on Precipitation: A Scientific Review*, Springer, New York.
- Lightly, J. S., J. M. Vernath, and A. F. Sarofim (2000), Combustion aerosols: Factors governing their size and composition and implications for human health, *J. Air Waste Manage. Assoc.*, *50*, 1565–1618.
- Low, R. D. H. (1969), A generalized equation for the solution effect in droplet growth, *J. Atmos. Sci.*, *26*, 1345–1346, doi:10.1175/1520-0469(1969)026<1345:R>2.0.CO;2.
- McDonald, J. E. (1953), Erroneous cloud-physics applications of Raoult's Law, *J. Meteorol.*, *10*, 68–70.
- McMurry, P. H., and M. R. Stolzenburg (1989), On the sensitivity of particle size to relative humidity for Los Angeles aerosols, *Atmos. Environ.*, *23*, 497–507, doi:10.1016/0004-6981(89)90593-3.
- Mikhailov, S., S. Vlasenko, T. Martin, T. Koop and U. Pöschl (2009), Amorphous and crystalline aerosol particles interacting with water vapor: conceptual framework and experimental evidence for restructuring, phase transitions and kinetic limitations, *Atmos. Chem. Phys.*, *9*, 9491–9522.
- Mita, A. (1979), A reexamination of the formula expressing the equilibrium water vapor pressure over an aqueous solution droplet, *J. Meteorol. Soc. Jpn.*, *57*, 79–83.
- Pagels, J., A. F. Khalizov, P. H. McMurry, and R. Y. Zhang (2009), Processing of soot by controlled sulphuric acid and water condensation—Mass and mobility relationship, *Aerosol Sci. Technol.*, *43*, 629–640, doi:10.1080/02786820902810685.
- Park, Y. J., H. S. Kim, and G. A. Jeffrey (1971), The crystal structure of 1, 6-Anhydro- $\beta$ -D-glycopyranose, *Acta Crystallogr., Sect. B Struct. Crystallogr. Cryst. Chem.*, *27*, 220–227, doi:10.1107/S0567740871001936.
- Petters, M. D., and S. M. Kreidenweis (2007), A single parameter representation of hygroscopic growth and cloud condensation nucleus activity, *Atmos. Chem. Phys.*, *7*, 1961–1971.
- Press, W. H., S. A. Teukolky, W. T. Vetterling, and B. P. Flannery (1992), *Numerical Recipes in C: The Art of Scientific Computing*, 2nd ed., Cambridge Univ. Press, Cambridge, U. K.
- Pruppacher, H. R., and J. D. Klett (1997), *Microphysics of Clouds and Precipitation*, Kluwer Acad., Dordrecht, Netherlands.
- Rissler, J., A. Vestin, E. Swietlicki, G. Fisch, J. Zhou, P. Artaxo, and M. O. Andreae (2006), Size distribution and hygroscopic properties of aerosol particles from dry-season biomass burning in Amazonia, *Atmos. Chem. Phys.*, *6*, 471–491.
- Roberts, G. C., and A. Nenes (2005), A continuous-flow streamwise thermal-gradient CCN chamber for atmospheric measurements, *Aerosol Sci. Technol.*, *39*, 206–221, doi:10.1080/027868290913988.
- Rose, D., S. S. Gunthe, E. Mikhailov, G. P. Frank, U. Dusek, M. O. Andreae, and U. Pöschl (2008), Calibration and measurement uncertainties of a continuous-flow cloud condensation nuclei counter (DMT-CCNC): CCN activation of ammonium sulfate and sodium chloride aerosol particles in theory and experiment, *Atmos. Chem. Phys.*, *8*, 1153–1179.
- Rosenørn, T., G. Kiss, and M. Bilde (2006), Cloud droplet activation of saccharides and levoglucosan particles, *Atmos. Environ.*, *40*, 1794–1802, doi:10.1016/j.atmosenv.2005.11.024.
- Saxena, V. K., J. N. Burford, and J. L. Kassner Jr. (1970), Operation of a thermal diffusion chamber for measurements on cloud condensation nuclei, *J. Atmos. Sci.*, *27*, 73–80, doi:10.1175/1520-0469(1970)027<0073:OOATDC>2.0.CO;2.
- Seinfeld, J. H., and S. N. Pandis (1998), *Atmospheric Chemistry and Physics*, 1326 pp., John Wiley, Hoboken, N. J.
- Shantz, N. C., W. R. Leitch, and P. F. Caffrey (2003), Effects of organics of low solubility on the growth rate of cloud droplets, *J. Geophys. Res.*, *108*(D5), 4168, doi:10.1029/2002JD002540.
- Snider, J. R., M. D. Petters, P. Wechsler, and P. Liu (2006), Supersaturation in the Wyoming CCN instrument, *J. Atmos. Oceanic Technol.*, *23*, 1323–1339, doi:10.1175/JTECH1916.1.
- Stevens, B., and G. Feingold (2009), Untangling aerosol effects on clouds and precipitation in a buffered system, *Nature*, *461*, 607–613, doi:10.1038/nature08281.
- Stratmann, F., A. Kiselev, S. Wurzler, M. Mendisch, J. Heinzenberg, R. J. Charlson, K. Diehl, H. Wex, and S. Schmidt (2004), Laboratory studies and numerical simulations of cloud droplet formation under realistic supersaturation conditions, *J. Atmos. Oceanic Technol.*, *21*, 876–887, doi:10.1175/1520-0426(2004)021<0876:LSANSO>2.0.CO;2.
- Stratmann, F., et al. (2010), Examination of laboratory-generated coated soot particles: An overview of the LACIS Experiment in November (LExNo) campaign, *J. Geophys. Res.*, *115*, D11203, doi:10.1029/2009JD012628.
- Stroud, C. A., et al. (2007), Cloud activating properties of aerosol observed during CELTIC, *J. Atmos. Sci.*, *64*, 441–459, doi:10.1175/JAS3843.1.
- Sullivan, R. C., M. J. K. Morre, M. D. Petters, S. M. Kreidenweis, G. C. Roberts, and K. A. Prather (2009), Effect of chemical mixing state on the hygroscopicity and cloud nucleation properties of calcium mineral dust particles, *Atmos. Chem. Phys.*, *9*, 3303–3316.
- Svenningsson, B., et al. (2006), Hygroscopic growth and critical supersaturations for mixed aerosol particles of inorganic and organic compounds of atmospheric relevance, *Atmos. Chem. Phys.*, *6*, 1937–1952.
- Tang, I. N., and H. R. Munkelwitz (1994), Water activities, densities, and refractive indices of aqueous sulfates and sodium nitrate droplets of atmospheric importance, *J. Geophys. Res.*, *99*, 18,801–18,808, doi:10.1029/94JD01345.
- Tao, Y., and P. H. McMurry (1989), Vapor pressures and surface free energies of C14–C18 monocarboxylic acids and C5 and C6 dicarboxylic acids, *Environ. Sci. Technol.*, *23*, 1519–1523, doi:10.1021/es00070a011.
- Textor, C., et al. (2006), Analysis and quantification of the diversities of aerosol life cycles within AeroCom, *Atmos. Chem. Phys.*, *6*, 1777–1813.
- Twomey, S. (1974), Pollution and the planetary albedo, *Atmos. Environ.*, *8*, 1251–1256, doi:10.1016/0004-6981(74)90004-3.
- Wallace, J. M., and P. V. Hobbs (2006), *Atmospheric Science: An Introductory Survey*, 2nd ed., 483 pp., Elsevier, New York.
- Warner, J., and S. Twomey (1967), The production of cloud nuclei by cane fires and the effect on cloud droplet concentration, *J. Atmos. Sci.*, *24*, 704–706, doi:10.1175/1520-0469(1967)024<0704:TPOCNB>2.0.CO;2.
- Wex, H., A. Kiselev, M. Ziese, and F. Stratmann (2006), Calibration of LACIS as a CCN detector and its use in measuring activation and hygroscopic growth of atmospheric aerosol particles, *Atmos. Chem. Phys.*, *6*, 4519–4527.
- Wex, H., T. Hennig, I. Salma, R. Ocskay, A. Kiselev, S. Henning, A. Massling, A. Wiedensohler, and F. Stratmann (2007), Hygroscopic growth and measured and modeled critical supersaturations of an atmospheric Hulis sample, *Geophys. Res. Lett.*, *34*, L02818, doi:10.1029/2006GL028260.
- Wex, H., M. D. Petters, C. M. Carrico, E. Hallbauer, A. Massling, G. R. McMeeking, L. Poulain, Z. Wu, S. M. Kreidenweis, and F. Stratmann (2009), Towards closing the gap between hygroscopic growth and activation for secondary organic aerosol: Part 1—Evidence from measurements, *Atmos. Chem. Phys.*, *9*, 3987–3997.
- Winklmayr, W., G. P. Reischl, A. O. Lindner, and A. Berner (1991), A new electromobility spectrometer for the measurement of aerosol size distributions in the size range from 1 to 1000 nm, *J. Aerosol Sci.*, *22*, 289–296, doi:10.1016/S0021-8502(05)80007-2.
- Young, K. C., and A. J. Warren (1992), A reexamination of the derivation of the equilibrium supersaturation curve for soluble particles, *J. Atmos. Sci.*, *49*, 1139–1143, doi:10.1175/1520-0469(1992)049<1138:AROTDO>2.0.CO;2.

M. Bilde, Department of Chemistry, University of Copenhagen, Universitetsparken 5, DK-2100 Copenhagen, Denmark.

M. Burkhardt and J. R. Snider, Department of Atmospheric Science, University of Wyoming, Dep. 3038, 1000 E. University Ave., Laramie, WY 82071, USA. (jsnider@uwyo.edu)

U. Dusek, Institute for Marine and Atmospheric Research, Utrecht University, Princetonplein 5, NL-3584 CC Utrecht, Netherlands.

G. P. Frank and A. Kristensson, Department of Physics, Lund University, Box 118, SE-22100 Lund, Sweden.

T. Hennig, Institute for Applied Environmental Science, Stockholm University, Svante Arrhenius väg 8, SE-10691 Stockholm, Sweden.

S. Henning, A. Kiselev, F. Stratmann, and H. Wex, Institute for Tropospheric Research, Department of Physics, Permoser Str. 15, D-04318, Leipzig, Germany.

A. Kiendler-Scharr and T. F. Mentel, ICG-II: Troposphere, Juelich Research Centre, D-52425 Juelich, Germany.

M. D. Petters, Department of Marine, Earth and Atmospheric Science, North Carolina State University, Raleigh, North Carolina, USA.

U. Pöschl and D. Rose, Biogeochemistry Department, Max Planck Institute for Chemistry, PO Box 3060, D-55020 Mainz, Germany.